Extra-field spike-timed activity shifts the place field center of mass to encode aversion experience

Omar Mamad[1,2], Beshoy Agayby[1,3,4], Lars Stumpp[1,3,4], Richard B. Reilly[1,3,4,5] and Marian Tsanov [1,2,*]

[1] Trinity College Institute of Neuroscience, Trinity College Dublin, Ireland

[2] School of Psychology, Trinity College Dublin, Ireland

[3]Trinity Centre for Bioengineering, Trinity College Dublin, Ireland

[4] School of Engineering, Trinity College Dublin, Ireland

[5] School of Medicine, Trinity College Dublin, Ireland

Correspondence: Marian Tsanov:

Trinity College Institute of Neuroscience, Trinity College Dublin, Dublin 2, Ireland

Fax: +353-1-896 3183; Tel: +353-1-896 4829; E-mail: tsanovm@tcd.ie

Running title: Extra-field place field activity encodes aversion

Abstract

The hippocampal neurons encode spatial representation but it remains unclear how they store concurrent positive or negative experiences. Here, we report a distinctive hippocampal code for contextual salient stimuli. We describe the plasticity rules governing CA1 place field reconfiguration in response to innately aversive trimethylthiazoline (TMT). We investigated if the place cells remap randomly or their reconfiguration depends on the location and timing of the aversive stimulus perception. The individual place fields followed a specific pattern: increased extra-field spiking in the TMT section during the aversive episodes resulted in larger shift of the place field center of mass. The induction of extra-field field plasticity was mediated by the basolateral amygdala complex (BLA). Optogenetic BLA-triggered increase of extra-field spiking activity in the photostimulation zone correlated to the degree of place field plasticity. We also applied closed-loop interface to test the hypothesis that the hippocampal remapping depends on the spike-timing proximity between the BLA activity and hippocampal spiking. Spike-timed optogenetic stimulation evoked significant shift of the center of mass only when the light pulses were delivered in a close temporal proximity to the neuronal spiking. Our findings underpin the spatial and temporal mechanisms of ensemble field reconfiguration triggered by aversive episodes.

Keywords: hippocampus, amygdala, optogenetics, place cells, brain-computer interface

Introduction

If we are ultimately to ameliorate the memories of traumatic events for the treatment of posttraumatic stress disorders we need to uncover how the aversive episodes rewire the brain connectivity. Hippocampus temporally encodes representations of spatial context-dependent experiences (Knierim 2003) and these memory traces are functionally strengthened in the cortical areas for long-term recollection (Nadel and Moscovitch 1997; Kitamura et al. 2009; Tayler et al. 2013; Denny et al. 2014). Current theories propose that memory of an event is represented by a population of neurons, referred to as engram (Ramirez et al. 2013; Josselyn et al. 2015; Tonegawa et al. 2015). Engrams engage overlapping neuronal populations for different memories (Cai et al. 2016; Rashid et al. 2016), such as the encoding of a single spatial environment with differing contextual emotional valences (Hsiang et al. 2014; Ye et al. 2016). Remapping of hippocampal place cells is a mechanism that generates multiple representations of a single unchanged spatial environment induced by non-spatial stimuli (Sharp 1999; Eichenbaum 2000). Aversion evokes field remapping (Moita et al. 2004; Kim et al. 2015) and a subset of neurons in hippocampal area CA1 change their preferred firing locations in response to predator odor (Wang et al. 2012). Despite recent advances in localizing and manipulating single engrams, it is still unclear which neurons remap to encode fearful experience and which neurons preserve their spatial fields. Here, we examined the rules governing aversion-induced place field remapping. We tested the hypothesis that the place cells remapping follows spatial and temporal pattern, which depends on the aversive stimulus perception. We examined the plasticity rules governing aversion-induced long-term shift of the place field center of mass (ΔCOM). The evaluation of ΔCOM is the most sensitive indicator of experience-dependent place field place field reconfiguration (Knierim 2002; Lee et al. 2004; Lee et al. 2006).

The amygdala supports aversive associative memories and relates adaptive behavior to the emotional valence of sensory stimuli (Phelps and LeDoux 2005; Sadrian and Wilson 2015). Amygdalar signaling of aversion controls the stability of hippocampal place cells and lesioning of the amygdala prevents the effect of fearful experience on the place fields remapping (Kim et al. 2015). Inactivation of amygdala blocks fear-conditioned tone stimulus that triggers place field remapping (Donzis et al. 2013), while amygdalar activation reduces the field stability of hippocampal place cells (Kim et al. 2012). Aversion-induced activation of the pyramidal neurons in amygdala mediates the formation of spatial context-dependent place aversion and in parallel with new hippocampal engrams (Ramirez et al. 2013; Ryan et al. 2015). However, there have been no direct tests of how new hippocampal ensembles are formed. To understand the mechanism of aversion-induced population response from hippocampal spatial representation we optogenetically activated pyramidal neurons from basolateral complex of amygdala (BLA). We photostimulated BLA to determine if the patterns of ensembles reconfiguration after aversion-induced place field remapping are replicated after optogenetic BLA activation. We investigated if the degree of place field plasticity differs when the spatial optogenetic stimulation was applied to the main place field compared to optogenetic stimulation of the extra-field activity with < 20% of the peak firing frequency (Brun et al. 2002). Extra-field spikes, previously considered to be noise, are now proposed to play an essential role in information processing, learning and memory formation (Johnson and Redish 2007; Johnson et al. 2009; Epsztein et al. 2011; Ferguson et al. 2011; Wu et al. 2017). Here, we explored if intra- or extra-filed spikes mediate experience-dependent encoding of aversive episodes. Finally, we applied closed-loop interface to test the hypothesis that the hippocampal remapping depends on the spike-timing proximity between the BLA activity and hippocampal spiking.

Results

Increase of hippocampal beta amplitude parallels TMT-mediated aversion episodes

To evoke an aversion episode for rats, chronically implanted with tetrodes in hippocampal CA1 region, we used 10% trimethylthiazoline (TMT) applied to restricted section (10x15 cm^2) of a rectangular-shaped linear track (Fig. 1A). TMT, a constituent of fox urine, is an innately aversive odor to rodents (Myers and Rinaman 2005; Kobayakawa et al. 2007). The experimental design consisted of three recording sessions (12 min each), conducted in the range of 48 hours: baseline recording (pre-TMT), recording with TMT located of one of the arms of the track (TMT) and subsequent recording without TMT (post-TMT). During the TMT session the animals (n = 12 rats) avoided to navigate across the TMT-scented section of the track (Fig. 1B, Supplementary Fig. 1A,B, Supplementary Movie 1), resulting in place avoidance (Fig. 1C, paired t-test, n = 12 rats, $t(11) = 10.4$, $P < 0.001$). The association of the TMT arms with the aversive odor was evident during the first minute of navigation in the post-TMT session (Fig. 1D, paired t-test, n = 12, $t(11) = -4.244$, $P = 0.001$). The average number of passes (2.58 ± 0.3) was significantly lower for the TMT arms compared to the anti-TMT arms (5.16 ± 0.7). To identify if the olfaction-mediated aversion was restricted to the TMT section of the maze or if it was occurring over the entire recording arena we analyzed the amplitude of hippocampal beta frequency band (15-40Hz, Fig. 1E, F) for each arm of the track (Fig. 1G). Successful odor discrimination is identified by hippocampal oscillations in beta frequency range (Igarashi et al. 2014) and aversive odors increase the amplitude of beta oscillations in rats (Chapuis et al. 2009). The hippocampal beta frequency (Supplementary Fig. 1C, one-way ANOVA, n = 12, $F_{(1,7)} = 3.8$, $P = 0.002$) and amplitude (Supplementary Fig. 1D, one-way ANOVA, n = 12, $F_{(1,7)} = 3.1$, $P = 0.005$) expressed dependence on the animal's whole body linear speed. Concurrently, the TMT-induced aversion slows down the linear speed (Supplementary Movie 1). To avoid

the bias of speed on beta parameters we analyzed the effect of TMT on beta oscillations for different speed bands. The highest increase of beta amplitude was evident during the passes on the arm with TMT odor (TMT arm 1, Fig. 1H, two-way ANOVA with Bonferroni post-hoc test, between groups, n = 12, $F_{(2,10)} = 17.5$, $P < 0.001$) with significant increase for five speed ranges. Significant beta amplitude increase was present also in the second arm between the food zones, adjacent to the TMT arm (TMT arm 2, Fig. 1I, two-way ANOVA with Bonferroni post-hoc test, between groups, $F_{(2,10)} = 24.3$, $P < 0.001$). The opposing loop between the food zones including anti-TMT arm 1 and anti-TMT arm 2 was characterized with non-significant changes of beta amplitude (Fig. 1J,K, two-way ANOVA with Bonferroni post-hoc test, between groups, n = 12, for anti-TMT arm 1: $F_{(2,10)} = 3.0$, $P = 0.094$ and for anti-TMT arm 2: $F_{(2,10)} = 1.3$, $P = 0.295$). We found no significant effect of TMT on the frequency of beta oscillation (Supplementary Fig. 1E, F, TMT arm 1: two-way ANOVA, between groups, with Bonferroni post-hoc correction, n = 12, $F_{(2,10)} = 0.7$, $P = 0.493$; TMT arm 2: n = 12, $F_{(2,10)} = 1.2$, $P = 0.349$; anti-TMT arm 1: n = 12, $F_{(2,10)} = 2.1$, $P = 0.164$; anti-TMT arm 2: n = 12, $F_{(2,10)} = 1.8$, $P = 0.213$.). These data indicate that the effect of TMT perception on the aversion behavior was restricted to one loop of the recoding arena that includes the TMT arms.

TMT biases the population code of spatial representation

We explored if the spatial representation of hippocampal fields is biased in respect to the TMT section of the track. For this we analyzed the center of mass from all place cells' spikes recorded from single animal using a spatial population vector (SPV), which estimates the Cartesian distribution of the spikes from multiple place fields. The SPV is based on place field rates, which represent spiking as a function of the occupancy for each pixel, thus the SPV is not biased by the time spent in particular section of the maze (Mamad et al. 2017). The SPV values

evaluate the spatial location of all place cells across main axis of the track, which is aligned between the two food corners (in degrees), where the SW corner is 0° and NE is 90° (Fig. 2A). We computed both weighted SPV (in which the cells are weighted by their firing rate) and averaged SPV (in which all cells are weighted equally). The TMT-exposed animals were split into two groups: a group with TMT located in the northeast loop of the track (NE-group, n = 6 rats, Fig. 2A) and a group in the southwest loop of the track (SW-group, n = 6 rats, Supplementary Fig. 2D). The NE-group showed a significant shift of the SPV values towards the NE section (Fig. 2B, Supplementary Fig. 2A) with weighted SPV of 53.3 ± 2.5° for post-TMT recording, compared to 44.9 ± 1.1° for pre-TMT recording (Supplementary Fig. 3D, TMT-NE group, paired t-test, n = 6, $t(5) = 3.8$, p = 0.012). Concurrently, the weighted SPV values of the SW-group shifted towards the SW section (Fig. 2E, Supplementary Fig. 2B) with weighted SPV of 38.9 ± 1.9° for post-TMT recording, compared to 44.1 ± 1.4° for pre-TMT recording (Supplementary Fig. 3E, paired t-test, n = 6, $t(5) = -2.6$, p = 0.047. *$P < 0.05$; between groups: Fig. 2C, pre-TMT comparison, unpaired t-test, n = 6, $t(10) = 0.47$, $P = 0.644$; post-TMT comparison, unpaired t-test, post weighted, n = 6, $t(10) = -4.48$, $P = 0.001$). Control group of animals did not show significant shift of SPV (Supplementary Fig. 3F, paired t-test, n = 6, $t(5) = -0.5$, p = 0.620). The change of the averaged SPV followed the similar patterns: 53.1 ± 2.0° for post-TMT recording, compared to 44.4 ± 1.7° for pre-TMT recording of the NE-group and 40.8 ± 1.9° for post-TMT recording, compared to 43.2 ± 1.6° for pre-TMT recording of the SW-group (Fig. 2F, pre-TMT comparison, unpaired t-test, pre averaged, n = 6, $t(10) = 0.52$, $P = 0.608$; post-TMT comparison, unpaired t-test, post averaged, n = 6, $t(10) = -4.43$, $P = 0.001$). These data show that aversive experience results in biased spatial representation of hippocampal place cell assemblies towards the location where it occurred.

The place cell's activity in the TMT arms during aversion episodes correlates to the degree of field reconfiguration

We examined if the individual place cells remap randomly of if they follow a spatial pattern. The stability of the recorded signal was verified with consistent spikes' amplitude and waveform across recording sessions (Supplementary Fig. 4A-D). The average shift of the center of mass (ΔCOM) between the pre-TMT and post-TMT recordings for the place fields from the TMT group was 12.44 ± 0.8 cm (Fig. 3A). This was a significant increase compared to the ΔCOM, examined from group of rats undergoing control recordings with neutral odor: 10% ethanol (Supplementary Fig. 5A,B), with baseline value of 6.32 ± 0.6 cm (unpaired t-test, control group n = 57, TMT group n = 106, $t(161) = 5.2$, $P < 0.001$). Furthermore, the ratio of the TMT- over anti-TMT number of passes for the first 60 seconds significantly correlated to the degree of ΔCOM (Fig. 3B, Pearson's r = -0.656, $P = 0.020$, n = 12). We investigated if the intra- and extra-field spiking activity of individual place cells during the TMT episodes (Fig. 3C) relates to subsequent shift of the place field center of mass angle (ΔCOMa). This parameter estimates the proximity of the center of mass to the TMT zone across the main axis of the track (see Methods & Materials), between 0° for SW corner and 90° for NE corner. The TMT session induced variable ΔCOMa between the pre-TMT and post-TMT sessions for the NE group of animals (Fig. 3D) as well as for the SW group of animals (Fig. 3E). We correlated the degree of ΔCOMa to the change of the firing rate of the place cells within the TMT arms. The change of the firing rate was calculated by the ratio of the baseline over the TMT session firing rate from the recorded spikes. We found significant negative correlation between ΔCOMa and the TMT spiking ratio of the mean firing rate measured for the TMT arms (Fig. 3F, Pearson's r = -0.276, $P = 0.004$, n = 106). Concurrently, no significance was evident for the correlation between ΔCOMa and the anti-TMT mean spiking ratio measured from the anti-TMT zone (Fig. 3G, Pearson's r = -0.016, p = 0.871, n = 106). Similarly, the correlation between ΔCOMa and

the spiking ratio of the peak firing rate was significant for the TMT arms (Fig. 3H, Pearson's r = -0.271, P = 0.005, n = 106), but not for the anti-TMT zone (Fig. 3I, Pearson's r = -0.083, P = 0.394, n = 106). In the control group of rats we found no significant correlation between ΔCOMa (Supplementary Fig. 5C,D) and the mean spiking ratio for the ethanol arms (Supplementary Fig. 6A, Pearson's r = -0.001, P = 0.997, n = 31) and for the anti-ethanol zone (Supplementary Fig. 6B, Pearson's r = -0.041, P = 0.822, n = 32). Similarly the correlations between ΔCOMa and peak spiking ration for both locations were non-significant (Supplementary Fig. 6C, Pearson's r = -0.092, P = 0.621, n = 31; Supplementary Fig. 6D, Pearson's r = -0.062, P = 0.734, n = 32). These data show that the cells' spiking during aversive episodes is related to subsequent place field remapping.

The rate of extra-field spiking during aversion episodes determines the degree of place field plasticity

We compared the field reconfiguration of the place cells with fields located in the TMT arms (with spiking ratio including intra-field spikes, Fig. 4A) to the remapping of the cells with place fields outside the TMT arms (with spiking ratio including only extra-field spikes, Fig. 4B). The place field was defined as the region of the arena in which the firing rate of the place cell was > 20% of the peak firing frequency (Brun et al. 2002). The extra-field TMT spiking ratio highly correlated to ΔCOMa for both the mean (Fig. 5A, Pearson's r = -0.465, P < 0.001, n = 54) and for the peak firing rate (Fig. 5E, Pearson's r = -0.453, P < 0.001, n = 54). However, the intra-field TMT spiking ratio showed no significant correlation to ΔCOMa for the mean firing rate (Fig. 5B, Pearson's r = 0.013, P = 0.925, n = 52) as well as for the peak firing rate (Fig. 5F, Pearson's r = -0.055, P = 0.698, n = 52). The dissociation of the spikes into TMT-extra- and intra-field groups had no effect for the place cells activity outside the TMT arms during the TMT sessions. No significant correlation was evident for the mean and peak firing rate of the

intra- (Fig. 5C, Pearson's r = -0.024, P = 0.864, n = 55; Fig. 5G, Pearson's r = -0.119, P = 0.387, n = 55) and extra-field spikes (Fig. 5D, Pearson's r = 0.027, P = 0.852, n = 52; Fig. 5H, Pearson's r = 0.062, P = 0.661, n = 52) in the anti-TMT zone. These results show that the degree of extra-field spiking increase during the TMT sessions predicts the degree of place field plasticity. Furthermore, the degree of extra-field spiking increase of these place cells during the TMT sessions predicted the degree of place field remapping.

BLA photostimulation mediates aversion-triggered shift of the center of mass

Basolateral amygdala (BLA) activation is known to trigger aversive behavior (Davis 1992). We investigated if BLA innervation of hippocampal mediates the aversion induced field plasticity and if optogenetic activation BLA excitatory neurons will exert effect similar to the TMT-evoked pattern of reconfiguration. To exert spatial control of the BLA neuronal activity we injected a viral construct AAV-CaMKIIα-hChR2-YFP in the BLA of Lister-Hooded rats (Fig. 6A). Delivery of blue light (473 nm) excited the spiking of neurons infected with AAV-CaMKIIα-hChR2-YFP (Fig. 6B,C) and induced concurrently aversive behavior (Supplementary Movies 2, 3). The majority of the photostimulated BLA neurons were CamKIIα-positive (Supplementary Fig. 7A). 87 ± 8% of neurons that expressed yellow fluorescent protein (YFP) also expressed CamKIIα, while 64 ± 5% of neurons that expressed CamKIIα also expressed YFP. We applied optogenetic stimulation (50Hz, trains of 12 pulses, 0.5Hz inter-train interval) in south and west arms of the track (ChR2 arms, Fig. 6D) and observed place avoidance in the ChR2 arms (Fig. 6E, paired t-test, n = 6 rats, $t(5) = 5.0$, P = 0.004). The psot-ChR2 session recollected the place aversion of the animals in the first minute of the recording (Fig. 6F, paired t-test, n = 6, $t(5) = -3.796$, p = 0.013).

BLA photostimulation affected the synchronization of hippocampal local field oscillations across the stimulation trials (Fig. 6G), where the power of the event-related potential increased in the range of 5 – 8 Hz (Fig. 6H). The phase-locking value is a parameter that measures the degree of local field synchrony between all stimulation epochs (see Materials & Methods). The phase-locking values were significantly higher for BLA light pulse delivery (Fig. 6I, 0.35 ± 0.04) compared to the shuffled BLA data (0.09 ± 0.07, paired t-test, n = 120 trials, $t(119) = 3.0$, $P = 0.005$), as well as compared to the control YFP group (0.01 ± 0.06, Supplementary Fig. 7F-H, unpaired t-test, n = 120 trials, $t(118) = 4.8$, $P = 0.009$). We next compared the change of the intra-field and extra-field spiking of place cells that fire in both ChR2-arms and anti-ChR2 zone. The spike count was examined in epochs of 100, 250, and 500ms pre- and post-BLA stimulation protocol onset. The positive value of the normalized count (0.03 ± 0.03) showed that the activation of the amygdala afferents resulted in a tendency of decreased intra-field spiking rate in the first 100ms post-BLA photostimulation (Fig. 6J). Concurrently, the extra-field spiking increased (represented by the negative value of the normalized count, -0.11 ± 0.04), which was significantly different from the extra-field normalized count for the first 100ms (paired t-test, n = 74 cells , $t(73) = 3.2$, $P = 0.002$), but not the 250ms (paired t-test, n = 74 cells, $t(73) = 1.1$, $P = 0.254$) and 500ms post-BLA photostimulation (paired t-test, n = 74 cells, $t(73) = 1.2$, $P = 0.247$). We compared the COM angle shift (ΔCOMa) between the pre- and post-ChR2 sessions for the place cells with fields located in the ChR2 arms (with intra-field spikes) and for the place cells with fields located in the anti-ChR2 zone (with extra-field spikes only). The average ΔCOMa of 7.57 ± 1.1 from cells with fields located in the ChR2 arms was significantly lower than ΔCOMa of 12.64 ± 1.6 from cells located in the anti-ChR2 zone (Fig. 6K, unpaired t-test, extra-field group, n = 38 cells, intra-field group, n = 42 cells, $t(78) = 5.0$, $P = 0.011$). ΔCOMa for the extra-filed spiking cells also differed significantly between the ChR2- and YFP (Supplementary Fig. 8A) control group of rats (unpaired t-test,

ChR2 intra-field group, n = 42 cells, YFP intra-field group, n = 32 cells, $t(72) = 5.3$, $P = 0.010$). The application of AAV-YFP in control rats evoked no electrophysiological (Supplementary Fig. 7B,C) or behavioral response (Supplementary Fig. 7D,E, paired t-test, n = 6 rats, $t(5) = 1.0$, $P = 0.358$). These data confirm BLA photoactivation as a reliable experimental protocol for behavioral place aversion and optogenetically-induced place field plasticity.

The extra-field spiking during BLA photostimulation predicts the center of mass shift

Place fields of the cells located in the anti-ChR2 zone that spiked during the photostimulation session (Fig. 7A) showed larger place field reconfiguration (Supplementary Movie 4), compared to the cells with little or no spiking activity (Fig. 7C). We correlated the COM angle shift (ΔCOMa) to the ratio of the baseline over the TMT session place cells' firing rate from the recorded spikes (ChR2 spiking ratio) for the place cells with fields located in the anti-ChR2 zone (with extra-field spikes) as well as for the place cells located in the ChR2 arms (with intra-field spikes, Fig. 8A). The mean and the peak extra-field ChR2 spiking ratios significantly correlated to ΔCOMa (Fig. 8C, Pearson's r = -0.429, $P = 0.007$; Fig. 8G, Pearson's r = -0.426, $P = 0.009$, n = 38). Concurrently, the mean and the peak intra-field ChR2 spiking ratio showed weak non-significant correlation to ΔCOMa for the ChR2 arms (Fig. 8E, Pearson's r = -0.261, $P = 0.099$; Fig. 8I, Pearson's r = -0.187, $P = 0.241$, n = 41). No significant correlation to ΔCOMa was evident for the mean and peak firing rate of the intra- (Fig. 8D, Pearson's r = 0.092, $P = 0.530$, n = 49; Fig. 8H, Pearson's r = 0.066, $P = 0.651$, n = 49) and extra-field spikes (Fig. 8F, Pearson's r = 0.099, $P = 0.529$, n = 42; Fig. 8J, Pearson's r = 0.032, $P = 0.842$, n = 42) for the anti-ChR2 zone. Similarly to the TMT protocol, the BLA photostimulation evoked varying degree of ΔCOMa even for the extra-field spiking cells. We examined if this variability depends on the timing between the CA1 neuronal spiking and the BLA activity.

BLA-evoked place field plasticity requires spike-timed photostimulation

To test the hypothesis that the temporal proximity between the amygdala activation and the place cell's firing affects the degree of field remapping we triggered spike-timed photostimulation to BLA fibers in dorsal CA1 (Fig. 9A). To apply consistently light pulses in a millisecond range following the spike generation of a selected place cell, we used closed-loop optogenetic photostimulation with brain computer interface (BCI, Fig. 9B). From each assembly-recording we have chosen a hippocampal place cell with a main place field and with extra-field spiking located in opposing arms of the track (Supplementary Movie 5). The closed-loop BCI evoked 5 ms blue light delivery immediately after the spike generation (1.25-2.31 ms) of the selected place cell (Supplementary Fig. 9A, B). The spikes from the selected place cells triggered 82.1 ± 4.4% of the BCI laser pulses, while 84.1 ± 3.8% of the triggered BCI laser pulses were evoked by the spikes from the selected place cells (Fig. 9C). The average shift of the center of mass (ΔCOM) between the pre-ChR2 and ChR2 recordings for the place fields of the BCI cells was 14.66 ± 2.3 cm after photostimulation with 50 Hz (Fig. 9D, Supplementary table 1). The residual non-BCI cells expressed significantly smaller value of 8.01 ± 0.7 cm (Fig. 9D, unpaired t-test, non-BCI cells n = 92, BCI cells n = 12, $t(102) = -3.04$, $P = 0.003$). We examined the effect of the closed-loop photostimulation on the field plasticity when the BCI was applied with delay of six seconds after the spike onset (Supplementary Fig. 9C). The timing of the delay allowed for photostimulation in random spatial locations across the track. The delayed cells expressed lower ΔCOM compared to the instant BCI cells (Fig. 9D, unpaired t-test, BCI cells n = 12, BCI delayed cells n = 12, $t(22) = 3.12$, $P = 0.005$). We found no significant difference between the BCI delayed cells with ΔCOM of 6.70 ± 0.9 cm for the BCI cells and the residual non-BCI cells with ΔCOM of 6.62 ± 0.5 (unpaired t-test, BCI delayed cells n = 12, non-BCI cells n = 122 cells, $t(132) = 0.83$, $P = 0.375$). Similarly to ΔCOM,

the change in the center of mass angle (ΔCOMa) was significantly larger for the BCI cells (Fig. 9E) from the instant ChR2 group (Fig. 10A) with value of 12.68 ± 1.9°, compared to the non-BCI cells (Fig. 10B) with 6.70 ± 0.7° ΔCOMa (unpaired t-test, non-BCI cells n = 92, BCI cells n = 12, $t(102) = -2.82$, $P = 0.006$). The average ΔCOMa of the BCI delayed cells (Fig. 10C, 6.70 ± 0.9°) was significantly smaller compared to the instant BCI cells (Supplementary table 1, unpaired t-test, BCI cells n = 12, BCI delayed cells n = 12, $t(22) = 2.74$, $P = 0.012$). Finally, the average ΔCOMa of the non-BCI cells (5.84 ± 0.5, Fig. 10D) did not differ significantly from to the ΔCOMa of the BCI delayed cells (unpaired t-test, BCI delayed cells n = 12, non-BCI cells n = 122 cells, $t(132) = 1.12$, $P = 0.117$). Our findings demonstrate that aversion-induced place field plasticity depends on the temporal proximity of BLA signal and place cell activity.

Discussion

In this study, we demonstrated the reconfiguration pattern of hippocampal place cells evoked by aversive episodes. We report that the place fields located outside the area of aversion express higher propensity for center of mass shift, compared to the fields located with the arms of the track associated with TMT-induced aversion. The degree of center of mass shift correlated with the firing rate of the extra-field spiking during the aversion. Optogenetic stimulation of extra-field spikes resulted in the same reconfiguration pattern with the exposure to innately aversive odor. BLA projections evoked field plasticity only after spatial and temporal proximity between the place cell's spikes and light delivery.

Beta amplitude increase displays the spatial location of aversive odor perception

The hippocampus is proposed to provide a contextual framework for the encoding of emotional events (Leutgeb et al. 2005). Recent data demonstrate that hippocampal spatial representation is not static but alters in response to non-spatial rewarding stimuli (Mamad et al. 2017). Hippocampal place cells remap also after exposure to stressful or fearful events (Moita et al. 2004; Kim et al. 2015). This remapping is a mechanism for the formation of new hippocampal engrams that store the association of spatial context and fearful experience (Ramirez et al. 2013; Tonegawa et al. 2015). Although population of place cells remap after exposure to stressful or fearful events (Moita et al. 2004; Kim et al. 2015), there is no clear explanation why some neurons alter their place fields to encode fearful experience, while others preserve stable fields. The application of innate aversive trimethylthiazoline (TMT) allowed us to study the transformation of hippocampal population code from neutral to negative context value for a single environment. The advantage of TMT is the absence of learning curve required for associative fear conditioning (Kobayakawa et al. 2007) and the absence of visible or tactile features of the environment that might affect the stability of the recorded place cells (Jeffery and O'Keefe 1999). Beta rhythm (15 – 40 Hz) is a characteristic oscillation in the olfactory bulb during odorant perception (Lowry and Kay 2007; Lepousez and Lledo 2013). During olfactory-driven behavior beta oscillations sustained long-range interactions between distant brain structures, including hippocampus (Martin et al. 2007). Entorhinal–hippocampal coupling was observed specifically in the 20 – 40 Hz frequency band as rats learned to use an odor cue to guide navigational behavior (Igarashi et al. 2014). The essence of beta rhythm in the processing of aversive stimuli across the limbic circuitry was demonstrated with the finding that powerful beta activity predicted the behavioral expression of conditioned odor aversion (Chapuis et al. 2009). Similarly, we showed that beta amplitude was increased during the TMT sessions, particularly in the TMT arms but not in the rest of the track. We revealed here that

beta rhythm varied as a function of speed, where the frequency of beta decreased, while the amplitude increased with the augmentation of the whole body motion of the animal.

Aversion experience reconfigures hippocampal place fields

After we identified the TMT arms as a section of the maze where the animals perceived the aversive stimulus, we compared the hippocampal spatial representation across the track axis, dissociating the TMT arms against the opposing arms. To evaluate if CA1 population response was biased across the axis of the maze we used a spatial population vector (SPV). The SPV was directed towards the TMT arms, showing that the majority of the remapped place field shifted their center of mass towards the section of the maze associated with aversive experience. SPV is described recently as a tool of a context-dependent modulation of spatial representation (Mamad et al. 2017), while the reconfiguration of individual place fields is best evaluated by the center of mass difference (Knierim 2002). We found that place fields from animals exposed to aversive TMT evoked higher center of mass change compared to control animals. Exposure to predator odor produces only partial remapping and one possibility is that the cells remaining stable encode visuospatial information, while the remapping cells are sensitive to other contextual cues such as olfactory information and/or emotional valence (Wang et al. 2012). Another possibility would be that spatial or temporal proximity of the neuronal activity to the perception of the aversive episode determine which place fields will reconfigure. To show that the spatial proximity to the olfactory stimulus was essential component of the field plasticity we compared the correlation between the change of the center of mass angle (ΔCOMa) and TMT spiking ratio within the TMT arms versus outside the TMT arms (anti-TMT zone). Surprisingly, we found that the first group (including intra-field spikes) showed no significant correlation, while the second group (including only extra-field spikes) highly correlated the spiking activity with the degree of center of mass shift. No significant

correlation was evident between ΔCOMa and intra- or extra-field spiking ration for the anti-TMT zone of the track. Although the contribution of extra-field spikes to spatial navigation is scarcely explored we know that their activity is crucially involved in hippocampus-dependent learning (Ferguson et al. 2011). The significance of the extra-field spikes is largely associated to the sharp-wave ripple replay of recently navigated locations and experiences (Wu et al. 2017), which are important in learning and memory consolidation during inactive behavioural state (Johnson et al. 2009). However, extra-field spikes from place cells have been shown to occur during active navigation (Johnson and Redish 2007; Epsztein et al. 2011). Here, we present evidence that the extra-filed activity encodes silent stimuli and if it is potent enough to evoke place field plasticity related to experience-dependent learning.

Amygdala mediates aversion-induced shift of the place field center of mass

The amygdala is a key structure in the acquisition of aversive experience (LeDoux 2000) and optogenetic stimulation of BLA mediates associative fear learning (Johansen et al. 2010; Klavir et al. 2017). The amygdala sets the emotional valence of sensory stimuli (Phelps and LeDoux 2005; Moriceau et al. 2006) and the BLA circuitry is particularly involved in the odor-evoked fear conditioning (Wallace and Rosen 2001; Anderson et al. 2003; de Araujo et al. 2003). The amygdala is critical for stress-induced modulation of hippocampal synaptic plasticity and hippocampus-dependent learning (Kim et al. 2001; Vouimba and Richter-Levin 2005). Aversion-triggered place cell remapping is blocked by amygdala inactivation (Donzis et al. 2013; Kim et al. 2015), while BLA stimulation decreases the stability of CA1 place fields (Kim et al. 2012). Despite recent advances in manipulating engrams (Cai et al. 2016; Rashid et al. 2016), there is no agreement if the place cells remap randomly or their reconfiguration depends on the location and timing of the aversive stimulus perception. We found that the BLA-triggered field plasticity pattern was equivalent to the TMT-induced field reconfiguration,

namely, the correlation between the ChR2 spiking ratio and ΔCOMa was significant only for place cells located outside the ChR2 arms. The observed reconfiguration pattern reveals that the increase of extra-field but not intra-field spiking during aversive episode predicts the change in the preferred firing location. Such response can emerge after a small, spatially uniform depolarization (Rickgauer et al. 2014) of the spatially untuned somatic membrane potential of inactive place cell leads to the sudden and reversible emergence of a spatially tuned subthreshold response and novel place field formation (Lee et al. 2012; Bittner et al. 2015). This phenomenon is proposed as a key mechanism for the formation of hippocampal memory representations (Lee et al. 2012). Our data complement these findings by showing that BLA stimulation increases only the extra-filed but not the intra-field spiking of the CA1 place cells.

Spike-timing is essential for the induction of place field plasticity

To test if temporal proximity between neuronal depolarization and synaptic inputs that provide aversive signals is potential predictor of field plasticity we used optogenetically-triggered activation of BLA fibers that innervate hippocampal place cells. To induce reliable spike-timed photostimulation we developed a BCI based on closed-loop pulse generation. The total BCI circuitry delay was 6.3-7.3 ms (including the 5 ms pulse duration). The timing of our pulse generation in respect to the postsynaptic depolarization falls well within the spike-timing dependent plasticity window of 40 ms (Markram et al. 1997; Froemke and Dan 2002). Our BCI design achieved great a degree of spike detection of 82.1 ± 4.4%, which was higher than previous report on closed-loop stimulation of hippocampal place cells with 52.9 ± 9.5% spike detection success rate (de Lavilleon et al. 2015). We found that BCI photostimulation of place cells evoked significantly higher degree of plasticity compared to the rest of recorded place cells (non-BCI neurons). Although this result was not surprising, it established the role of the temporal proximity for field plasticity and it explained the variability of ΔCOMa observed

previously in the TMT- and ChR2 arms. Spike-timed depolarization may underline not only the encoding of aversive but also of rewarding or salient stimuli mediated by the subcortical or entorhinal projections to hippocampus (Harvey et al. 2009). We propose that this pattern of field reconfiguration serves as a universal mechanism for the generation of multiple context-dependent representations by different salient stimuli, where the animal's behavior is guided by the contextual valence of previous experience.

Materials and Methods

Ethics Statement

We conducted our experiments in accordance with directive 2010/63/EU of the European Parliament and of the council of 22 September 2010 on the protection of animals used for scientific purposes and the S.I. No. 543 of 2012, and followed Bioresources Ethics Committee, Trinity College Dublin, Ireland (individual authorization number AE19136/I037; Procedure Numbers 230113-1001, 230113-1002, 230113-1003, 230113-1004 and 230113-1005), and international guidelines of good practice, under the supervision of Marian Tsanov, who is licensed by the Irish Medical Board (project authorization number: AE19136/P003).

Animals

Male, 3-6 months old, Lister-Hooded rats were individually housed for at least 7 days before all experiments, under a 12-h light–dark cycle, provided with water *ad libitum*. Rats were food deprived to 80% of their original weight. Experiments were performed during the light phase.

Surgical implantation of recording electrodes and recording techniques

Eight tetrodes and otic fiber were implanted in hippocampal CA1 area: -3.8 AP, 2.3 ML and 1.8 mm dorsoventral to dura. Optic fiber and tetrodes were implanted unilaterally in BLA: 2.4 AP, 4.9 ML, and 7.0 mm dorsoventral to dura. The recordings were performed as previously described (Mamad et al. 2015). After a minimum 1 week recovery, subjects were connected, via a 32-channel headstage (Axona Ltd.), to a recording system, which allowed simultaneous animal position tracking. Signals were amplified (10000- to 30000-fold) and band-pass filtered between 380 Hz and 6 kHz for single-unit detection. To maximize cell separation, only waveforms of sufficient amplitude (at least three times the noise threshold) were recorded. Candidate waveforms were discriminated off-line using graphical software (Tint, Axona Ltd.), which allows waveform separation based on multiple features including spike amplitude, spike duration, maximum and minimum spike voltage, and the time of occurrence of maximum and minimum spike voltages. Autocorrelation histograms were calculated for each unit, and the unit was removed from further analysis if the histogram presented spiking within the first 2 ms (refractory period), inconsistent with good unit isolation. Only stable recordings across consecutive days were further analyzed. The stability of the signal was evaluated by the cross-correlation of spike amplitudes and similarity comparison of the spike clusters between the sessions. Electrode stability was assessed off-line by comparison of waveforms and cluster distributions. The single unit signals of the last recording session and the probe were compared for waveform similarity, cluster location, size, and boundaries. Peak and trough amplitudes of the averaged spike waveforms were compared by Pearson's *r*. R values ≥ 0.8 indicated that the same populations of cells were recorded throughout the last recording session and the probe.

Hippocampal unit identification and spatial firing analysis

Single hippocampal pyramidal cells and interneurons were identified using spike shape and firing frequency characteristics (Wilson and McNaughton 1993). Firing rate maps allow for visual inspection of neurons preferred areas of firing (i.e. place fields). They were constructed

by normalizing the number of spikes which occurred in specific pixelated coordinates by the total trial time the animal spent in that pixel. This produced maps depicting the place fields of each cell and quantified in Hz (smoothed maps). We defined place field size as the region of the arena in which the firing rate of the place cell was greater than 20% of the maximum firing frequency (Brun et al. 2002). Appearance of sharp waves and ripples during immobility, triggers the spiking of multiple place cells (Wu et al. 2017). To avoid spikes reactivation during sharp wave ripple we excluded spikes that occurred during epochs with running speeds below 5 cm/s (Alme et al. 2014; Grosmark and Buzsaki 2016). The place field analysis included only epochs during which the animal's velocity was at least 5 cm/s.

Extra-field spiking

Place fields were defined as areas of 9 contiguous pixels (2.5 cm^2 / pixel) with average activity >20% of the field maximum rate. Extra-field spiking was defined as spikes occurring outside of the identified place field areas (Huxter et al. 2003; Johnson and Redish 2007). The extra-filed spiking thus includes secondary place fields with sizes smaller than 9 contiguous pixels or with averaged firing rate smaller than 20% of the maximum firing rate (Brun et al. 2002; Huxter et al. 2003; Johnson and Redish 2007).

Measurement of local field activity.

The local field potential (LFP) was sampled at 250 Hz and stored for further off-line analysis. LFP signal frequency analysis was done using MATLAB's Signal Processing Toolbox (MATLAB, Natick, MA) where the power was calculated using the short-time Fourier transform of the signal (hanning window of 2s, with overlap of 1 s) and interpolated into colour-coded power spectrograms. Information was displayed as the magnitude of the time-dependent Fourier transform versus time in a color gradient graph with the maximum corresponding to 0 Db.

Phase-locking value

To evaluate the effect of optogenetic BLA stimulation we compared the hippocampal local field oscillations of a single electrode between multiple trials (Mamad et al. 2015). Phase-locking statistics measures the significance of the phase covariance between separate signals and allows direct quantification of frequency-specific synchronization (i.e., transient phase-locking) between local field potentials (Lachaux et al. 1999). The phase-locking value is the amplitude of the first circular moment of the measured phase difference between two phases (Lachaux et al. 1999; Canolty et al. 2010). The phase-locking value ranges between 0 and 1; 0 signifying purely random rise and fall whereas a value of 1 signifies that one signal perfectly follows the other. To distinguish between noise-related fluctuations of the phase-locking values we compared the observed data with shuffled data (Mamad et al. 2015).

Experimental design

The animals were trained to navigate between the northwest and southeast corners, where two pellets were continuously positioned. The animals were allowed to navigate in both clockwise and anti-clockwise directions of the rectangular-shaped linear track (10cm width, 85cm length of the arms). For the TMT experiments one of the filter papers of the track was scented with 50 µl 10% trimethylthiazoline (Contech). The advantage of trimethylthiazoline (TMT) is the absence of learning curve required for associative fear conditioning and the absence of visible or tactile features of the environment that might affect the stability of the recorded place cells. The experimental protocol involving one TMT session with duration of 12 min was designed to evoke long-lasting (>24 hours) but weak place aversion response during the post-TMT recording session. The place aversion was measured only in the first 60 seconds of the post-TMT recording session. In the subsequent 11 minutes of the post-TMT recording session the animals displayed compensatory navigation in the TMT arms. This protocol allowed for

sufficient number of passes, preventing an undersampling path measurement of the post-TMT navigation. During the TMT sessions the TMT filter papers were applied in all locations of the TMT arms for different rats; this protocol was designed to match the ChR2 protocol where the blue light was applied across all locations of the ChR2 arms. For the optic stimulation sessions, the laser was switched on when the animal entered the south arm or the west arm with continuous photostimulation trains (473 nm, 50 Hz, 5 ms pulse duration, 12 pulses per train, 0.5 sec inter-train interval) until the animal exited this section of the track. The blue laser was synchronized with the video-tracking and with the recoding system through DACQBASIC scripts (Axona. Ltd). The duration of each session (baseline, TMT, ChR2) was 12 min. The TMT zone (ChR2 zone) included the TMT arms (ChR2 arms) and the feeding corners. For control experiments we used filter papers of the track scented with 50 µl 10% ethanol, which was a familiar odor to the rats. The animals were habituated prior the recording sessions to the scent of 10% ethanol.

Virus construction and optical activation

AAV-CaMKIIa-hChR2(H134R)-eYFP-WPRE-hGH viral construct was serotyped with AAV5 coat proteins and packaged by Vector Core at the University of North Carolina with viral titers ranged from 1.5-8 x 10^{12} particles per mL. For control experiments we used virus bearing only the YFP reporter. Randomization of group allocation (ChR2 versus YFP controls) was performed using an online randomization algorithm (http://www.randomization.com/). The virus injection was applied unilaterally in the BLA (2.4 AP, 4.9 ML), with volume of 2µl injected on two levels: 1µl at 6.5 mm and 1µl at 7.5 mm dorsoventral to the dura. Subsequently an optical fiber (200 µm core diameter, Thorlabs, Inc.) was chronically inserted (2.4 AP, 4.9 ML, 6.5 DV). Simultaneous optical stimulation and extracellular recording from CA1 were performed in freely-behaving rats 3 weeks after the surgery. For the closed-loop BLA experiment with concurrent recordings in the hippocampal CA1 region the optical fiber was

inserted inside the microdrive cannula (Axona, Ltd.) of the recording tetrodes, with the tip of the tetrodes projecting beyond the fiber by 500 μm, and the optical fiber was coupled to a 473 nm laser (Thorlabs, Inc.). The light power was controlled to be 10-15 mW at the fiber tip. Square-wave pulses with duration of 5 ms were delivered at frequency of 50Hz.

Spiking ratios

$$TMT\ spiking\ ratio = \frac{firing\ rate\ from\ the\ pre - TMT\ session\ in\ the\ TMT\ arms}{firing\ rate\ from\ the\ TMT\ session\ in\ the\ TMT\ arms}$$

$$Anti - TMT\ SR\ = \frac{firing\ rate\ from\ the\ pre - TMT\ session\ in\ the\ anti - TMT\ zone}{firing\ rate\ from\ the\ TMT\ session\ in\ the\ anti - TMT\ zone}$$

$$TMT\ /anti\ TMT\ passes\ ratio = \frac{Number\ of\ passes\ in\ the\ TMT\ arms}{Number\ of\ passes\ in\ the\ anti - TMT\ arms}$$

$$ChR2\ spiking\ ratio = \frac{firing\ rate\ from\ the\ pre - ChR2\ session\ in\ the\ ChR2\ arms}{firing\ rate\ from\ the\ ChR2\ session\ in\ the\ ChR2\ arms}$$

$$ChR2\ /\ anti\ ChR2\ passes\ ratio = \frac{Number\ of\ passes\ in\ the\ ChR2\ arms}{Number\ of\ passes\ in\ the\ anti - ChR2\ arms}$$

$$Pre\ /\ post\ normalized\ spikes\ count = \frac{(spikes\ count\ pre - spikes\ count\ post)}{(spikes\ count\ pre + spikes\ count\ post)}$$

Center of Mass

The center of mass of the place cells' spike distribution is calculated as follows:

$$COM_x = \frac{\sum_{i=1}^{N_x}\sum_{j=1}^{N_y} f_{ij} \cdot i}{\sum_{i=1}^{N_x}\sum_{j=1}^{N_y} f_{ij}} \cdot l_{bin} - \frac{l_{bin}}{2}$$

$$COM_y = \frac{\sum_{i=1}^{N_x}\sum_{j=1}^{N_y} f_{ij} \cdot j}{\sum_{i=1}^{N_x}\sum_{j=1}^{N_y} f_{ij}} \cdot l_{bin} - \frac{l_{bin}}{2}$$

Where N_x, N_y define the number of bins in the arena in X-, Y- direction; $f_{i,j}$ is firing frequency in bin i, j; l_{bin} is the bin-size.

Given the origin O (O_x,O_y), which denotes the northwest (SE) corner of the Cartesian coordinate system, and the direction of the symmetry axis D (D_x,D_y), which denotes the line between the southwest (SW) and northeast (NE) corners, the distance of the COM (COM_x,COM_y) to the symmetry axis is calculated as follows:

$$dist_{COM/sym} = \frac{\left| det \begin{bmatrix} D_x - O_x & D_y - O_y \\ COM_x - O_x & COM_y - O_y \end{bmatrix} \right|}{\sqrt{(P_x - O_x)^2 + \left(D_y - O_y\right)^2}}$$

Where P is the shortest distance between the COM and the symmetry line. For the rectangular-shaped linear track, the arena borders are defined as the square surrounding all motion tracking sample points with an equal distance to the real limits of the arena at all sides.

Using $dist_{COM}$ we calculate the distance between O and P as follows:

$$\overline{OP} = \sqrt{({COM_x}^2 + {COM_y}^2) - {dist_{COM}}^2}$$

The COM distance normalized by the arena width perpendicular to the symmetry axis through the COM is:

$$dist_{norm} = \left\{ \begin{matrix} \dfrac{dist_{COM}}{\overline{OP} \cdot C}, \overline{OP} < \dfrac{\overline{OM}}{2} \\ \dfrac{dist_{COM}}{(\overline{OM} - \overline{OP}) \cdot C}, \overline{OP} > \dfrac{\overline{OM}}{2} \end{matrix} \right\}$$

Where $\overline{OM}$ is the diagonal of a square inclosing all motion tracking data points, and C is a motion tracking data factor set to 0.85 for the linear rectangular track.

Center of Mass Angle

The COM angle (COMa) is calculated as follows:

$$\theta_{COM} = \begin{Bmatrix} 45° \cdot (1 - dist_{norm}), COM_x < COM_y \\ 45° \cdot (1 + dist_{norm}), COM_x > COM_y \end{Bmatrix}$$

Where θ_{COM} is center of mass angle; COM_x, COM_y : X-, Y- coordinate of COM, $dist_{norm}$ normalized COM distance.

Delta center of mass is the absolute difference between the pre- and post-TMT(ChR2) recordings:

$$|\Delta COM| = COM_{(pre\text{-}TMT)} - COM_{(post\text{-}TMT)}$$

$$|\Delta COM| = COM_{(pre\text{-}ChR2)} - COM_{(post\text{-}ChR2)}$$

Spatial population vector

We used population vector of the place field distribution *D* as well as the grand rate population vector *F* to describe the common behaviour of the whole population of place cells recorded. The population vector of place field distribution consists of the COM-angle of each cell $\theta_{COM,n}$ where n indicates the cell index:

$$D_n = \theta_{COM,n}$$

$$F_n = \frac{s_n}{\Delta t_{tot}}$$

Where S_n is number of spikes of cell *n*; Δt_{tot} is duration of the measurement.

The spatial population vector weighted by the mean firing frequency of the cells $SPV_{weighted}$ is calculated as the dot-product of the grand rate population vector *F* and the population vector of place field distribution *D* normalized by the 1-norm of the grand rate population vector:

$$SPV_{weighted} = \frac{F \cdot D}{\|F\|_1}$$

And the average spatial population vector SPV_{avg} is defined as the 1-norm of the population vector of place field distribution *D*, normalised by the number of place cells *N* in the population:

$$SPV_{avg} = \frac{\|D\|_1}{\mathrm{N}}$$

The 1-norm of a vector is defined as the sum of its elements:

$$\|F\|_1 = \sum_{n=1}^{N} |F_n| \,;\; \|D\|_1 = \sum_{n=1}^{N} |D_n|$$

All algorithms were created using MATLAB.

Brain-computer interface

For optogenetic BCI stimulation of amygdala fibers the closed-loop interface evoked photostimulation that was triggered immediately after spike detection of a chosen place cell. Alternatively, the BCI protocol was initiated after delay of 6 seconds. 6 sec delay results in non-spike-timed photostimulation in random area of the track. The signal from the headstage was processed to the Preamp/ADC unit with differential amplifiers and analogue to digital converter (ADC), allowing for digital filtering of the signal. The signal then is processed in system unit (Axona Ltd.) with digital signal processing (DSP) microprocessor that allows the filtering of the single units with a band-pass filter with the limits 360 Hz and 7 kHz. The filtered data are then transferred to the computer via USB interface and outputted as an audio signal when a spike is detected. Computer with installed DacqUSB system (Axona Ltd.) enables audio monitoring of the spikes detected during single-unit recording. Audio output from the system unit is connected to comparator circuitry through a 3.5 mm connector. A simple first-order low pass filter using resistors and capacitors (RC circuit) was used to reduce the effect of the noise on the signal. The comparator circuit is composed of an operational amplifier (OPA2244PA). The comparator circuit used a threshold for square pulse generation. An output signal of 5 volts

was initiated when the input was higher than the programmed threshold. This digital output was then processed in an Arduino UNO board (Arduino). The UNO board is a microcontroller board including a microcontroller (ATmega328P0) that is operated by a 16 MHz quartz crystal. The Arduino allows for open-source hardware and an integrated development environment (IDE) based on C++ programming. The microcontroller was programmed to operate in a loop in which it checks for a high digital input from the comparator; if such an input arrives, a stimulation pulse is produced. The stimulation pattern was programmed with a pulse duration of 5 ms pulse followed by a 10 ms pause. This pattern was chosen because of the kinetics of the used channelrhodopsin (ChR2); at least 5 ms is required to achieve proper neuron activation (Nagel et al. 2003; Boyden et al. 2005; Yizhar et al. 2011) and 10 ms of no stimulation to avoid sustained depolarization (Mattis et al. 2011). The output of the Arduino was fed towards the laser for stimulation with a parallel output towards data acquisition system. A data acquisition system (Labjack U12) recorded the onsets of the stimulation modulation pulses produced by the Arduino board to compare the matching of the stimulation signal to the recorded single-unit spikes. In-house scripts written in MATLAB (MathWorks, Inc., USA) were used for timing analysis of closed-loop BCI. The script analyzed the data from the single unit recording and the stimulation signal to determine 1) the percentage of the stimulation pulses that were triggered by the recorded spikes from selected place cell and 2) the percentage of the spikes from the selected place cell that successfully evoked stimulation pulses.

The delay of transferring the signal from the recoding electrodes to the system unit is 1-2 ms (dacqUSB User Manual). This delay is due to the digital signal processing that takes place in the Preamp/ADC unit of the dacqUSB system to filter the raw data. Subsequent 200 μs delay within the system unit to process the signal. A delay of of 39.5 (± 22.9) μs for the low pass filter was estimated as the time difference between the input and the output of the filter when each reached the value of the threshold used in the comparator (0.13 volts). A delay with an

average value of 12.9 (± 2.4) μs was estimated for the comparator processing, while a delay with an average value of 32.4 (± 4.7) μs was estimated the Arduino UNO board processing. The total BCI circuit delay from neural spike generation to stimulation pulse generation was in the range of 1.25-2.31 ms. This timing falls within the spike-timing dependent plasticity window of +10 ms (Markram et al. 1997; Sjostrom et al. 2001; Yao and Dan 2001).

Histology

At the end of the study, brains were removed for histological verification of electrode localization. Rats were deeply anesthetized with sodium pentobarbital (390 mg/kg) and perfused transcardially with ice-cold 0.9% saline followed by 4% paraformaldehyde. Brains were removed, post-fixed in paraformaldehyde for up to 24 hours and cryoprotected in 25% sucrose for >48 hours. Brains were sectioned coronally at 40μm on a freezing microtome. Primary antibody incubations were performed overnight at 4°C in PBS with BSA and Triton X-100 (each 0.2%). The concentration for primary antibodies was anti-CamKIIα 1:500 (Millipore, # 05-532). Sections were then washed and incubated in PBS for 10 minutes and secondary antibodies were added (1:500) conjugated to Alexa Fluor 594 dye (Invitrogen, # A11032) for 2 hours at room temperature.

For visualization, the sections were mounted onto microscope slides in phosphate-buffered water and cover-slipped with Vectashield mounting medium. The YFP fluorescence was evaluated within a selected region that was placed below the fiber tip in an area of 1.5mm x 1.5mm. Fluorescence was quantified based on the average pixel intensity within the selected region (Witten et al. 2011). The stained sections were examined with Olympus IX81 confocal microscope at 594nm for Alexa Fluor secondary antibody and 488nm for ChR2-YFP. CamKIIα-positive neurons were identified based on expression of red fluorescence, whereas ChR2-positive neurons were identified by expression of green fluorescence. Co-localization of

Alexa Fluor 594 and YFP was determined manually using ImageJ software (Image Processing and Analysis in Java).

Statistical Analysis

Two different approaches were used to calculate the sample size (Karalis et al. 2016). We performed power analyses to establish the required number of rats for experiments in which we had sufficient data on response variables. For experiments in which the outcome of the intervention could not be predetermined, we used a sequential stopping rule. This approach allows null-hypothesis tests to be used subsequently by analyzing the data at different experimental stages using *t*-tests against type II error. The experiment was initiated with four animals per group; if the P reached value below 0.05, the testing was continued with two or three more animals to increase the statistical power. In case of $P > 0.36$, the experiment was discontinued and the null hypothesis was accepted (Karalis et al. 2016). All data were analyzed using SPSS Software. Statistical significance was estimated by using a two-tailed independent samples *t*-test for non-paired data or a paired samples Student *t*-test for paired data. Repeated measures were evaluated with two-way analysis of variance (ANOVA) paired with *post hoc* Bonferroni test. Correlations between data sets were determined using Pearson's correlation coefficient. The probability level interpreted as significant was fixed at $p < 0.05$. Data points are plotted ± sem.

Data Availability

Dataset of all experimental files is available at Figshare public repository, DOI: 10.6084/m9.figshare.5336026 with URL: https://figshare.com/s/da6864eb8fadaa7fd6ba.

Acknowledgements

This work was supported by Science Foundation Ireland, the Health Research Board and the Wellcome under Biomedical Research Partnership, grant #099926/Z/12/Z to Marian Tsanov.

Competing interests

The authors declare no competing financial interests.

References

Alme CB, Miao C, Jezek K, Treves A, Moser EI, Moser MB. 2014. Place cells in the hippocampus: eleven maps for eleven rooms. Proc Natl Acad Sci U S A 111:18428-18435.

Anderson AK, Christoff K, Stappen I, Panitz D, Ghahremani DG, Glover G, Gabrieli JD, Sobel N. 2003. Dissociated neural representations of intensity and valence in human olfaction. Nat Neurosci 6:196-202.

Bittner KC, Grienberger C, Vaidya SP, Milstein AD, Macklin JJ, Suh J, Tonegawa S, Magee JC. 2015. Conjunctive input processing drives feature selectivity in hippocampal CA1 neurons. Nat Neurosci 18:1133-1142.

Boyden ES, Zhang F, Bamberg E, Nagel G, Deisseroth K. 2005. Millisecond-timescale, genetically targeted optical control of neural activity. Nat Neurosci 8:1263-1268.

Brun VH, Otnaess MK, Molden S, Steffenach HA, Witter MP, Moser MB, Moser EI. 2002. Place cells and place recognition maintained by direct entorhinal-hippocampal circuitry. Science 296:2243-2246.

Cai DJ, Aharoni D, Shuman T, Shobe J, Biane J, Song W, Wei B, Veshkini M, La-Vu M, Lou J, Flores SE, Kim I, Sano Y, Zhou M, Baumgaertel K, Lavi A, Kamata M, Tuszynski M, Mayford M, Golshani P, Silva AJ. 2016. A shared neural ensemble links distinct contextual memories encoded close in time. Nature 534:115-118.

Canolty RT, Ganguly K, Kennerley SW, Cadieu CF, Koepsell K, Wallis JD, Carmena JM. 2010. Oscillatory phase coupling coordinates anatomically dispersed functional cell assemblies. Proc Natl Acad Sci U S A 107:17356-17361.

Chapuis J, Garcia S, Messaoudi B, Thevenet M, Ferreira G, Gervais R, Ravel N. 2009. The way an odor is experienced during aversive conditioning determines the extent of the network recruited during retrieval: a multisite electrophysiological study in rats. J Neurosci 29:10287-10298.

Davis M. 1992. The role of the amygdala in fear and anxiety. Annu Rev Neurosci 15:353-375.

de Araujo IE, Rolls ET, Kringelbach ML, McGlone F, Phillips N. 2003. Taste-olfactory convergence, and the representation of the pleasantness of flavour, in the human brain. Eur J Neurosci 18:2059-2068.

de Lavilleon G, Lacroix MM, Rondi-Reig L, Benchenane K. 2015. Explicit memory creation during sleep demonstrates a causal role of place cells in navigation. Nat Neurosci 18:493-495.

Denny CA, Kheirbek MA, Alba EL, Tanaka KF, Brachman RA, Laughman KB, Tomm NK, Turi GF, Losonczy A, Hen R. 2014. Hippocampal memory traces are differentially modulated by experience, time, and adult neurogenesis. Neuron 83:189-201.

Donzis EJ, Rennaker RL, Thompson LT. 2013. Fear conditioning alters neuron-specific hippocampal place field stability via the basolateral amygdala. Brain Res 1525:16-25.

Eichenbaum H. 2000. Hippocampus: mapping or memory? Current biology : CB 10:R785-787.
Epsztein J, Brecht M, Lee AK. 2011. Intracellular determinants of hippocampal CA1 place and silent cell activity in a novel environment. Neuron 70:109-120.
Ferguson JE, Jackson JC, Redish AD. 2011. An inside look at hippocampal silent cells. Neuron 70:3-5.
Froemke RC, Dan Y. 2002. Spike-timing-dependent synaptic modification induced by natural spike trains. Nature 416:433–438.
Grosmark AD, Buzsaki G. 2016. Diversity in neural firing dynamics supports both rigid and learned hippocampal sequences. Science 351:1440-1443.
Harvey CD, Collman F, Dombeck DA, Tank DW. 2009. Intracellular dynamics of hippocampal place cells during virtual navigation. Nature 461:941-946.
Hsiang HL, Epp JR, van den Oever MC, Yan C, Rashid AJ, Insel N, Ye L, Niibori Y, Deisseroth K, Frankland PW, Josselyn SA. 2014. Manipulating a "cocaine engram" in mice. J Neurosci 34:14115-14127.
Huxter J, Burgess N, O'Keefe J. 2003. Independent rate and temporal coding in hippocampal pyramidal cells. Nature 425:828-832.
Igarashi KM, Lu L, Colgin LL, Moser MB, Moser EI. 2014. Coordination of entorhinal-hippocampal ensemble activity during associative learning. Nature 510:143-147.
Jeffery KJ, O'Keefe JM. 1999. Learned interaction of visual and idiothetic cues in the control of place field orientation. Exp Brain Res 127:151-161.
Johansen JP, Hamanaka H, Monfils MH, Behnia R, Deisseroth K, Blair HT, LeDoux JE. 2010. Optical activation of lateral amygdala pyramidal cells instructs associative fear learning. Proc Natl Acad Sci U S A 107:12692-12697.
Johnson A, Fenton AA, Kentros C, Redish AD. 2009. Looking for cognition in the structure within the noise. Trends Cogn Sci 13:55-64.
Johnson A, Redish AD. 2007. Neural ensembles in CA3 transiently encode paths forward of the animal at a decision point. J Neurosci 27:12176-12189.
Josselyn SA, Kohler S, Frankland PW. 2015. Finding the engram. Nat Rev Neurosci 16:521-534.
Karalis N, Dejean C, Chaudun F, Khoder S, Rozeske RR, Wurtz H, Bagur S, Benchenane K, Sirota A, Courtin J, Herry C. 2016. 4-Hz oscillations synchronize prefrontal-amygdala circuits during fear behavior. Nat Neurosci 19:605-612.
Kim EJ, Kim ES, Park M, Cho J, Kim JJ. 2012. Amygdalar stimulation produces alterations on firing properties of hippocampal place cells. J Neurosci 32:11424-11434.
Kim EJ, Park M, Kong MS, Park SG, Cho J, Kim JJ. 2015. Alterations of hippocampal place cells in foraging rats facing a "predatory" threat. Current biology : CB 25:1362-1367.
Kim JJ, Lee HJ, Han JS, Packard MG. 2001. Amygdala is critical for stress-induced modulation of hippocampal long-term potentiation and learning. J Neurosci 21:5222-5228.
Kitamura T, Saitoh Y, Takashima N, Murayama A, Niibori Y, Ageta H, Sekiguchi M, Sugiyama H, Inokuchi K. 2009. Adult neurogenesis modulates the hippocampus-dependent period of associative fear memory. Cell 139:814-827.
Klavir O, Prigge M, Sarel A, Paz R, Yizhar O. 2017. Manipulating fear associations via optogenetic modulation of amygdala inputs to prefrontal cortex. Nat Neurosci.
Knierim JJ. 2002. Dynamic interactions between local surface cues, distal landmarks, and intrinsic circuitry in hippocampal place cells. J Neurosci 22:6254-6264.
Knierim JJ. 2003. Hippocampus and memory. Can we have our place and fear it too? Neuron 37:372-374.
Kobayakawa K, Kobayakawa R, Matsumoto H, Oka Y, Imai T, Ikawa M, Okabe M, Ikeda T, Itohara S, Kikusui T, Mori K, Sakano H. 2007. Innate versus learned odour processing in the mouse olfactory bulb. Nature 450:503-508.

Lachaux JP, Rodriguez E, Martinerie J, Varela FJ. 1999. Measuring phase synchrony in brain signals. Human brain mapping 8:194-208.
LeDoux JE. 2000. Emotion circuits in the brain. Annu Rev Neurosci 23:155-184.
Lee D, Lin BJ, Lee AK. 2012. Hippocampal place fields emerge upon single-cell manipulation of excitability during behavior. Science 337:849-853.
Lee I, Griffin AL, Zilli EA, Eichenbaum H, Hasselmo ME. 2006. Gradual translocation of spatial correlates of neuronal firing in the hippocampus toward prospective reward locations. Neuron 51:639-650.
Lee I, Rao G, Knierim JJ. 2004. A double dissociation between hippocampal subfields: differential time course of CA3 and CA1 place cells for processing changed environments. Neuron 42:803-815.
Lepousez G, Lledo PM. 2013. Odor discrimination requires proper olfactory fast oscillations in awake mice. Neuron 80:1010-1024.
Leutgeb S, Leutgeb JK, Barnes CA, Moser EI, McNaughton BL, Moser MB. 2005. Independent codes for spatial and episodic memory in hippocampal neuronal ensembles. Science 309:619-623.
Lowry CA, Kay LM. 2007. Chemical factors determine olfactory system beta oscillations in waking rats. J Neurophysiol 98:394-404.
Mamad O, McNamara HM, Reilly RB, Tsanov M. 2015. Medial septum regulates the hippocampal spatial representation. Frontiers in behavioral neuroscience 9:166.
Mamad O, Stumpp L, McNamara HM, Ramakrishnan C, Deisseroth K, Reilly RB, Tsanov M. 2017. Place field assembly distribution encodes preferred locations. PLoS Biol 15:e2002365.
Markram H, Lubke J, Frotscher M, Sakmann B. 1997. Regulation of synaptic efficacy by coincidence of postsynaptic APs and EPSPs. Science 275:213–215.
Martin C, Beshel J, Kay LM. 2007. An olfacto-hippocampal network is dynamically involved in odor-discrimination learning. J Neurophysiol 98:2196-2205.
Mattis J, Tye KM, Ferenczi EA, Ramakrishnan C, O'Shea DJ, Prakash R, Gunaydin LA, Hyun M, Fenno LE, Gradinaru V, Yizhar O, Deisseroth K. 2011. Principles for applying optogenetic tools derived from direct comparative analysis of microbial opsins. Nature methods 9:159-172.
Moita MA, Rosis S, Zhou Y, LeDoux JE, Blair HT. 2004. Putting fear in its place: remapping of hippocampal place cells during fear conditioning. J Neurosci 24:7015-7023.
Moriceau S, Wilson DA, Levine S, Sullivan RM. 2006. Dual circuitry for odor-shock conditioning during infancy: corticosterone switches between fear and attraction via amygdala. J Neurosci 26:6737-6748.
Myers EA, Rinaman L. 2005. Trimethylthiazoline supports conditioned flavor avoidance and activates viscerosensory, hypothalamic, and limbic circuits in rats. Am J Physiol Regul Integr Comp Physiol 288:R1716-1726.
Nadel L, Moscovitch M. 1997. Memory consolidation, retrograde amnesia and the hippocampal complex. Curr Opin Neurobiol 7:217-227.
Nagel G, Szellas T, Huhn W, Kateriya S, Adeishvili N, Berthold P, Ollig D, Hegemann P, Bamberg E. 2003. Channelrhodopsin-2, a directly light-gated cation-selective membrane channel. Proc Natl Acad Sci U S A 100:13940-13945.
Phelps EA, LeDoux JE. 2005. Contributions of the amygdala to emotion processing: from animal models to human behavior. Neuron 48:175-187.
Ramirez S, Liu X, Lin PA, Suh J, Pignatelli M, Redondo RL, Ryan TJ, Tonegawa S. 2013. Creating a false memory in the hippocampus. Science 341:387-391.
Rashid AJ, Yan C, Mercaldo V, Hsiang HL, Park S, Cole CJ, De Cristofaro A, Yu J, Ramakrishnan C, Lee SY, Deisseroth K, Frankland PW, Josselyn SA. 2016. Competition between engrams influences fear memory formation and recall. Science 353:383-387.

Rickgauer JP, Deisseroth K, Tank DW. 2014. Simultaneous cellular-resolution optical perturbation and imaging of place cell firing fields. Nat Neurosci 17:1816-1824.
Ryan TJ, Roy DS, Pignatelli M, Arons A, Tonegawa S. 2015. Memory. Engram cells retain memory under retrograde amnesia. Science 348:1007-1013.
Sadrian B, Wilson DA. 2015. Optogenetic Stimulation of Lateral Amygdala Input to Posterior Piriform Cortex Modulates Single-Unit and Ensemble Odor Processing. Front Neural Circuits 9:81.
Sharp PE. 1999. Complimentary roles for hippocampal versus subicular/entorhinal place cells in coding place, context, and events. Hippocampus 9:432-443.
Sjostrom PJ, Turrigiano GG, Nelson SB. 2001. Rate, timing, and cooperativity jointly determine cortical synaptic plasticity. Neuron 32:1149–1164.
Tayler KK, Tanaka KZ, Reijmers LG, Wiltgen BJ. 2013. Reactivation of neural ensembles during the retrieval of recent and remote memory. Current biology : CB 23:99-106.
Tonegawa S, Liu X, Ramirez S, Redondo R. 2015. Memory Engram Cells Have Come of Age. Neuron 87:918-931.
Vouimba RM, Richter-Levin G. 2005. Physiological dissociation in hippocampal subregions in response to amygdala stimulation. Cereb Cortex 15:1815-1821.
Wallace KJ, Rosen JB. 2001. Neurotoxic lesions of the lateral nucleus of the amygdala decrease conditioned fear but not unconditioned fear of a predator odor: comparison with electrolytic lesions. J Neurosci 21:3619-3627.
Wang ME, Wann EG, Yuan RK, Ramos Alvarez MM, Stead SM, Muzzio IA. 2012. Long-term stabilization of place cell remapping produced by a fearful experience. J Neurosci 32:15802-15814.
Wilson MA, McNaughton BL. 1993. Dynamics of the hippocampal ensemble code for space. Science 261:1055-1058.
Witten IB, Steinberg EE, Lee SY, Davidson TJ, Zalocusky KA, Brodsky M, Yizhar O, Cho SL, Gong S, Ramakrishnan C, Stuber GD, Tye KM, Janak PH, Deisseroth K. 2011. Recombinase-driver rat lines: tools, techniques, and optogenetic application to dopamine-mediated reinforcement. Neuron 72:721-733.
Wu CT, Haggerty D, Kemere C, Ji D. 2017. Hippocampal awake replay in fear memory retrieval. Nat Neurosci 20:571-580.
Yao H, Dan Y. 2001. Stimulus timing-dependent plasticity in cortical processing of orientation. Neuron 32:315–323.
Ye L, Allen WE, Thompson KR, Tian Q, Hsueh B, Ramakrishnan C, Wang AC, Jennings JH, Adhikari A, Halpern CH, Witten IB, Barth AL, Luo L, McNab JA, Deisseroth K. 2016. Wiring and Molecular Features of Prefrontal Ensembles Representing Distinct Experiences. Cell 165:1776-1788.
Yizhar O, Fenno LE, Davidson TJ, Mogri M, Deisseroth K. 2011. Optogenetics in neural systems. Neuron 71:9-34.

Figures and Figure Legends

Figure 1:

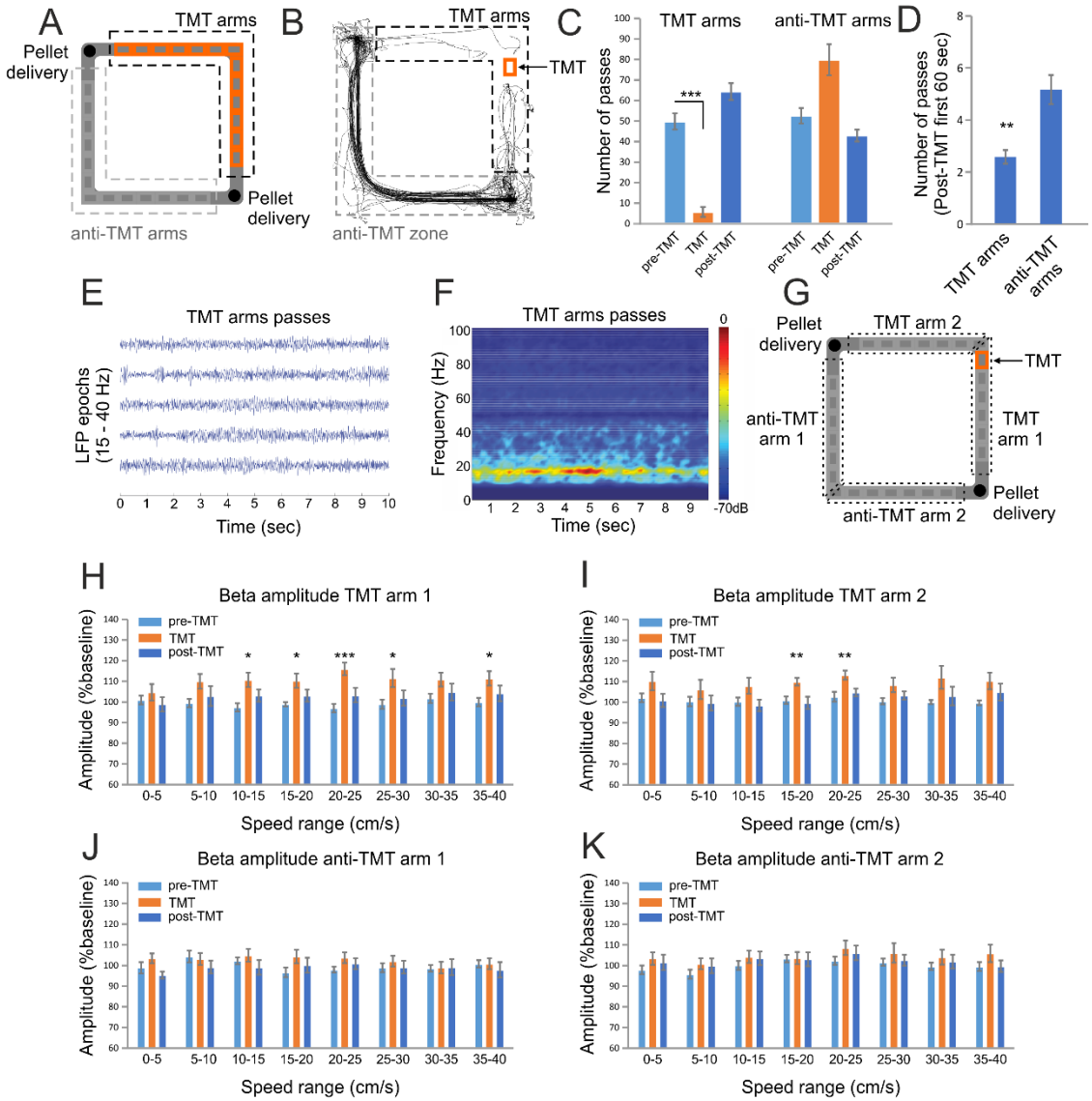

Figure 1. Hippocampal beta amplitude increase during odor-triggered place avoidance. (A) Behavioral set-up of rectangular-shaped linear track. Locations of the TMT are marked with red in the north and east arms of the track. The black dashed line indicates the TMT arms, while grey dashed line marks the anti-TMT arms. To match the TMT protocol with the subsequent ChR2 photostimulation protocol we applied the TMT scent papers to all locations across the TMT arms. (B) Navigation path of sample animal during the TMT session. Note the place avoidance of the TMT arms. The grey dashed line marks the anti-TMT zone. (C) Number

of passes counted in the TMT arms vs anti-TMT arms during the pre-TMT-, TMT- and post-TMT sessions, ***$P < 0.001$. Error bars, mean ± s.e.m. (D) Number of passes through the TMT- and anti-TMT arms for the first 60 seconds of the post-TMT session. **$P < 0.01$. (E) Representative band pass filtered (15 – 14Hz) local field potential (LFP) recorded during the passes in the TMT arms. Time 0 indicates the onset of the path trajectory starting from pellet delivery location. (F) Representative averaged band pass filtered (15 – 40Hz) color-coded power spectrogram of all TMT arms passes. Time 0 indicates the onset of the path trajectory starting from pellet delivery location. The averaged power-spectrogram includes the variability of passes duration and speed during the navigation across the arms. (G) Spatial dissociation of odor perception. The arm with TMT scent paper (marked with red) was named TMT arm 1. The adjacent arm, part of the same food-navigation loop, was TMT arm 2. The opposite of the TMT arm 1 was named anti-TMT arm 1, while the opposite of the TMT arm 2 was anti-TMT arm 2. The scent was detected by the animal at different locations during the navigation passes across the TMT arms. (H) Beta amplitude for TMT arm 1 and (I) TMT arm 2 (right) as percent of the pre-TMT session values for the entire track. ***$P < 0.001$, **$P < 0.01$, *$P < 0.05$ Error bars, mean ± s.e.m. (J) Beta amplitude for anti-TMT arm 1 and (K) anti-TMT arm 2 as percent of the pre-TMT session values for the entire track. The amplitude values are presented as a function of the animal's whole body speed, where beta amplitude is evaluated for speed range of 0 – 40 cm/s in bins of 5 cm/s. Error bars, mean ± s.e.m.

Figure 2:

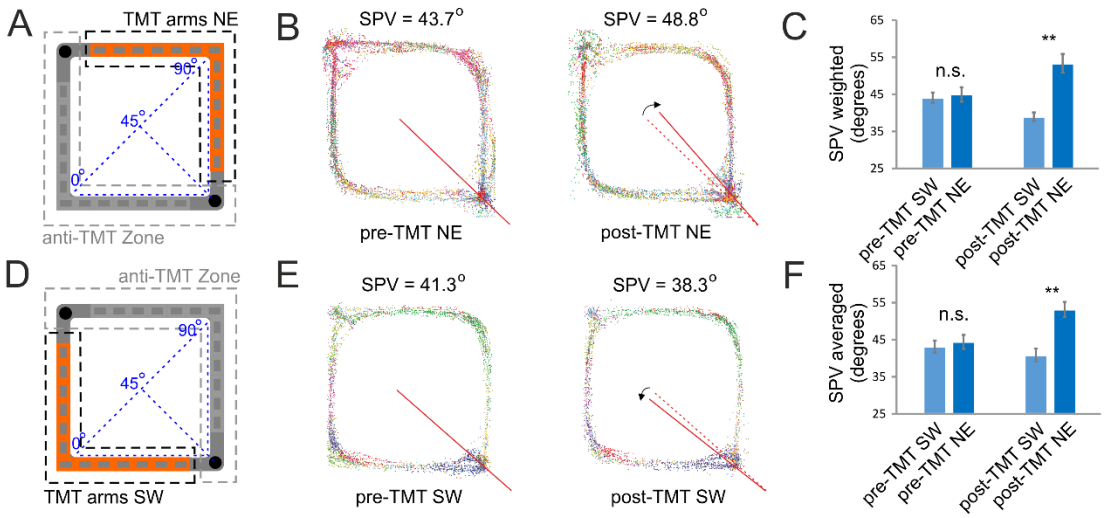

Figure 2. Place field assembly redistribution after TMT aversion experience. (A) Schematic representation of the TMT arms position (marked with red) in the rectangular-shaped linear track for animals exposed to TMT in the north or east arms of the track (NE group of animals). The representation of the Spatial Population Vector (SPV) coordinates between the SW and NE corner of the track is marked with dashed blue line, where SW corner is 0° and NE is 90°. The SPV values evaluate the spatial location of all place cells across the main axis of the track. The same coordinates are used for the subsequent evaluation of the center of mass angle (COMa). (B) Spatial distribution of the spikes (colored dots) of CA1 place cells (represented by different colors) recorded during pre-TMT (left panel) and post-TMT recording session (right panel) from sample animal from the NE-group. The straight red line denotes the weighted SPV between SW at 0° and NE at 90°. The dashed red line in the post-TMT session shows the SPV of the pre-TMT session. (C) Comparison of the weighted SPV between SW- (light blue) and NE-group of animals (dark blue) for pre- (left) and post-TMT sessions (right). $^{**}P < 0.01$. Error bars, mean ± s.e.m. (D) Schematic representation of the TMT arms position (marked with red) in the rectangular-shaped linear track for animals exposed to TMT in the south or west arms of the track (SW group of animals). SPV coordinates between the SW and

NE corner of the track are marked with dashed blue line, where SW corner is 0° and NE is 90°. (E) Spatial distribution of the spikes (colored dots) of CA1 place cells (represented by different colors) recorded during pre-TMT (left panel) and post-TMT recording session (right panel) from a sample animal from the SW-group. (F) Comparison of the averaged SPV between SW- (light blue) and NE-group of animals (dark blue) for pre- (left) and post-TMT sessions (right). $^{**}P < 0.01$. Error bars, mean ± s.e.m.

Figure 3:

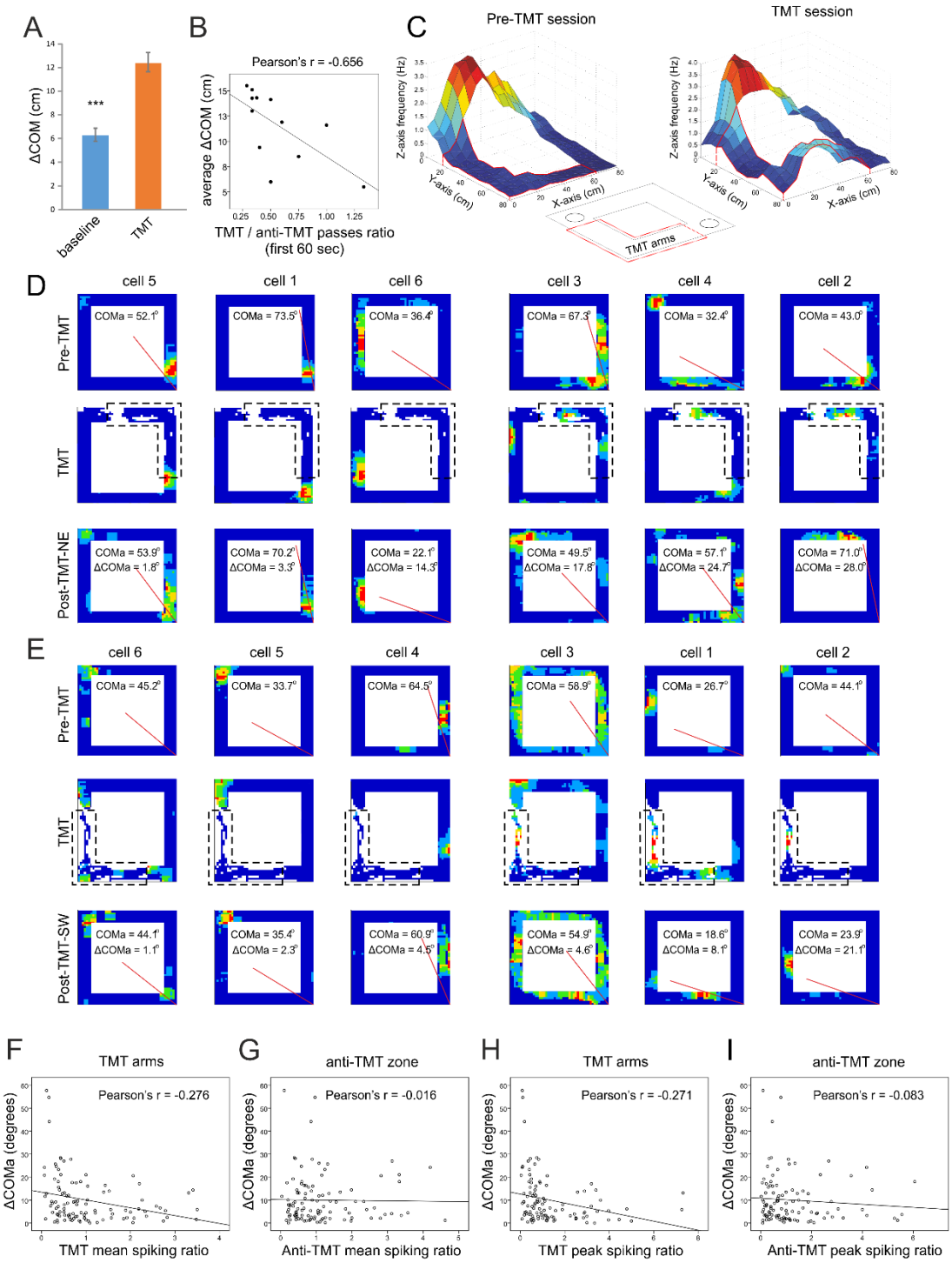

Figure 3. Individual place field reconfiguration after exposure to TMT. (A) Center of mass shift (ΔCOM) of place cells recorded from baseline group of animals exposed to neutral familiar odor (10% ethanol) and group of rats exposed to innately aversive odor (10% TMT).

***$P < 0.001$. Error bars, mean ± s.e.m. (B) Correlation between the average ΔCOM for each rat and the ratio of the TMT- over the anti-TMT arms passes for the first 60 seconds of the post-TMT session. (C) Left: Color-coded 3D-spatial map of a sample place cell with place field located outside the TMT arms (the TMT arms are marked with red line), recorded during pre-TMT session. X- and Y-axes represent the coordinates of the recording arena, while Z-axis represents the firing rate of the recorded neuron. Blue colors represent low-, while red colors represent high firing rate. Right: Color-coded 3D-spatial map of a sample place cell with place field located outside the TMT arms (the TMT arms are marked with red line), recorded during TMT session. The inset below shows with red line the position of the TMT arms (circles indicate the pellet delivery corners). The spiking TMT ratio represents the mean (peak) firing rate of the pre-TMT session over the TMT session. (D) Six sample place cells recorded from animal of the NE group during pre-TMT session (upper panels), TMT session (middle panels) and post-TMT session (lower panels). The straight red line denotes the center of mass angle (COMa) for each cell between SW at 0° and NE at 90°. For better visualization of the COMa, the rate map was restricted to the track coordinates. Note that some of the place cells exhibited higher firing rate in the TMT arms during the TMT sessions (panels positioned on the right half) compared to place cells with little or no spiking (panels positioned on the left half). (E) Six sample place cells recorded from animal of the SW group during pre-TMT session, TMT session and post-TMT session. For better visualization of the COMa, the rate map was restricted to the track coordinates. (F) Correlation between ΔCOMa and TMT spiking ratio based on the mean firing rate of the place cells' spikes in the TMT arms. (G) Correlation between ΔCOMa and anti-TMT spiking ratio based on the mean firing rate of the place cells' spikes in the anti-TMT zone. (H) Correlation between ΔCOMa and the spiking ratio based on the peak firing rate for the spikes in the TMT arms. (I) Correlation between ΔCOMa and the spiking ratio based on the peak firing rate for the spikes in the anti-TMT zone.

Figure 4:

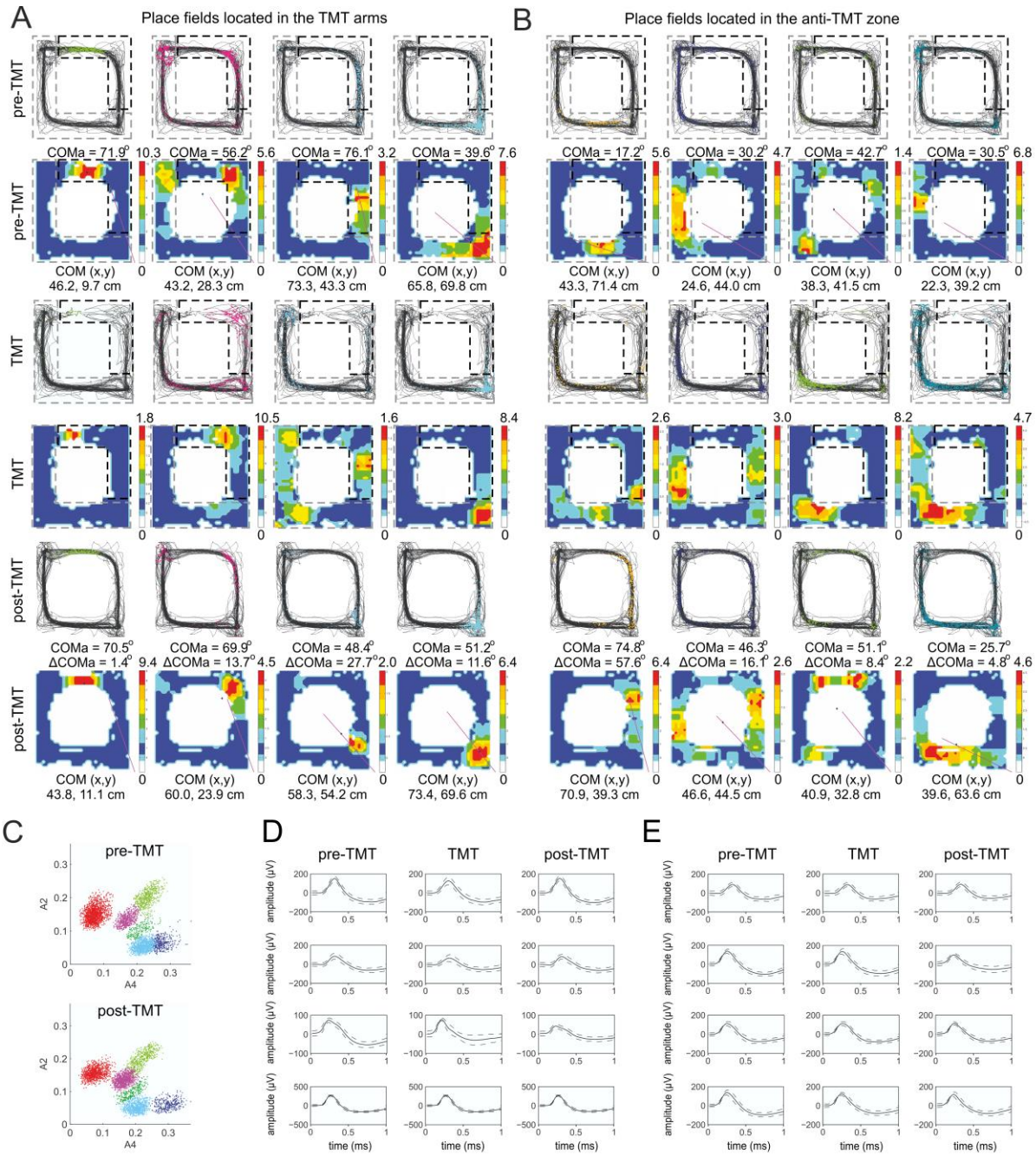

Figure 4. Comparison between intra- and extra-field place cells spiking during TMT exposure. (A) Four place fields from sample animal with fields located in the TMT arms during pre-TMT sessions (top), TMT (middle) and post-TMT sessions (bottom). For each session the upper panels show the animal trajectory with spikes, marked with colored dots, while the lower panels show color-coded firing rate. (B) Four place fields from the same animal with fields

outside the TMT arms. (C) Scatterplot, showing the signals from six units recorded between two pairs of electrodes on a given tetrode from a pre-TMT (left) and post-TMT session (right). The color-coded clusters represent the spikes from individual units at the scatterplot. (D) Waveforms of the place cells from the pre-TMT, TMT and post-TMT sessions shown in A, and (E) waveforms of the cells shown B, respectively. The solid line shows the average waveform shape; the dashed lines show the 1 SD confidence intervals.

Figure 5:

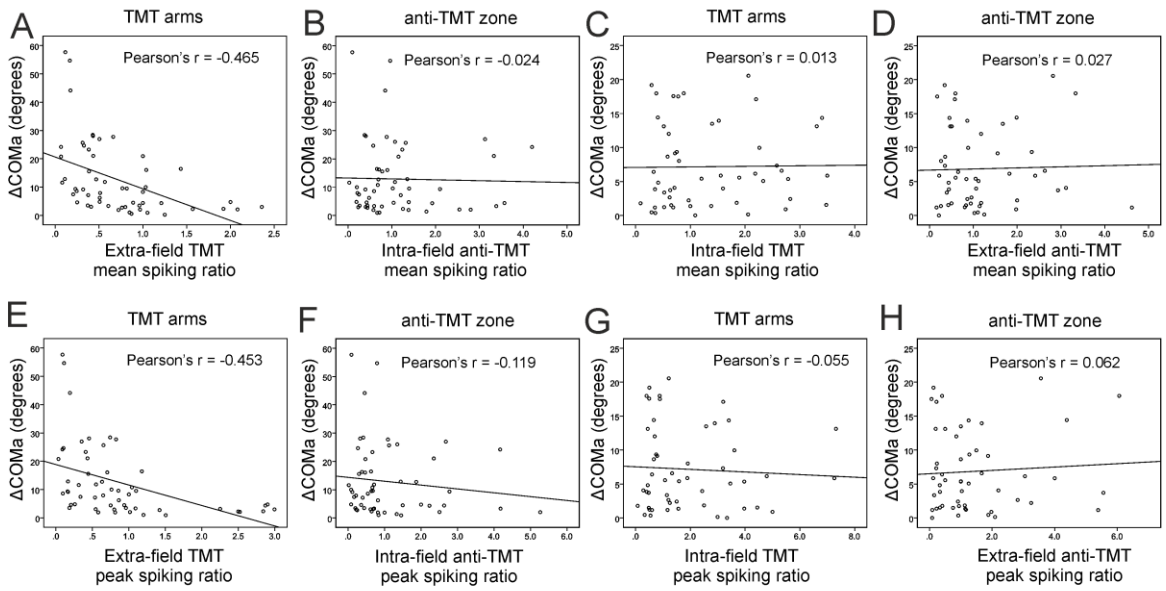

Figure 5. Increased extra-field place cell spiking during TMT exposure predicts spatial field reconfiguration. (A) Correlation between ΔCOMa and TMT mean spiking ratio for the place cells located outside the TMT arms (extra-field spikes). (B) Correlation between ΔCOMa and anti-TMT mean spiking ratio for the place cells located inside the anti-TMT arms (intra-field spikes). (C) Correlation between ΔCOMa and TMT mean spiking ratio for the place cells located inside the TMT arms (intra-field spikes). (D) Correlation between ΔCOMa and anti-TMT mean spiking ratio for the place cells located outside the anti-TMT zone (extra-field spikes). (E) Correlation between ΔCOMa and TMT peak spiking ratio for the place cells located outside the TMT arms (extra-field spikes). (F) Correlation between ΔCOMa and anti-TMT peak spiking ratio for the place cells located inside the anti-TMT zone (intra-field spikes). (G) Correlation between ΔCOMa and TMT peak spiking ratio for the place cells located inside the TMT arms (intra-field spikes). (H) Correlation between ΔCOMa and anti-TMT peak spiking ratio the place cells located outside the anti-TMT zone (extra-field spikes).

Figure 6:

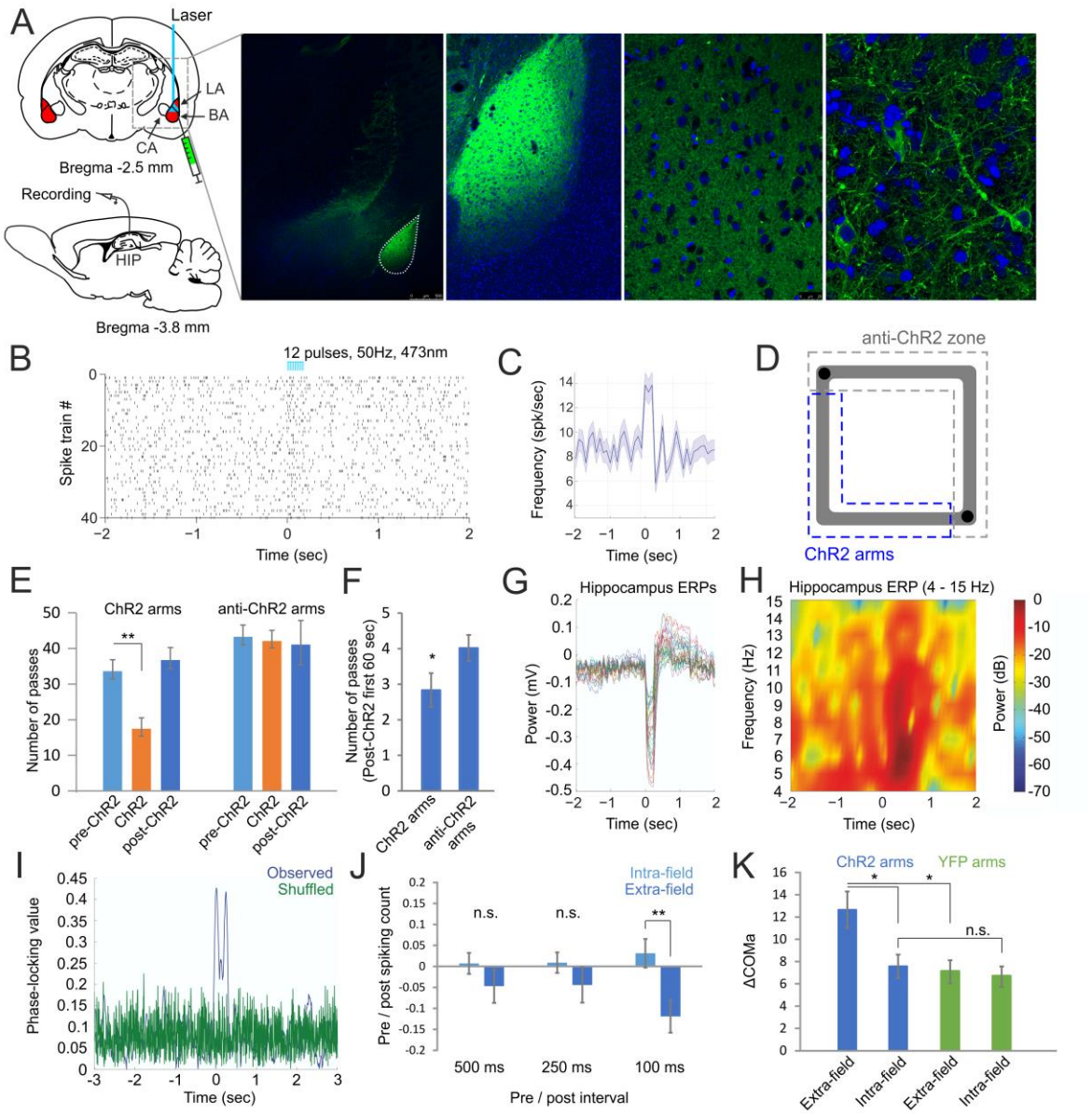

Figure 6. Photostimulation of basolateral complex of amygdala evokes spatial aversion. (A) Atlas schematic shows the injection site of AAV-CaMKIIα-hChR2-YFP and the optic fiber location in the basolateral complex of amygdala (BA – basal nucleus, LA – lateral nucleus of amygdala, CA – central nucleus of amygdala). The confocal images on the right show increasing levels of magnification of the YFP-expressing neurons (green) in BLA is histology with DAPI staining (blue). (B) Raster plot from 40 repetitions and (C) averaged firing frequency of optically evoked time-locked excitation of a BLA cell. Time 0 indicates the

delivery of the first train of the stimulation protocol. (D) Experimental setup: light delivery in the south and west ChR2 arms, marked with dashed blue line. (E) Number of passes counted in the ChR2 arms vs anti-ChR2 arms during the pre-ChR2, ChR2- and post-ChR2 sessions. $^{**}P < 0.01$. Error bars, mean ± s.e.m. (F) Number of passes through the ChR2- and anti-ChR2 arms for the first 60 seconds of the post-ChR2 session. (G) Event related potentials (ERPs) recorded in dorsal CA1 from of 32 electrodes in a sample animal. Time 0 indicates the delivery of the onset of the BLA optogenetic stimulation. (H) Color-coded power spectrogram of hippocampal low-frequency oscillations (4 – 15Hz) during the photostimulation protocol. (I) Representative phase-locking value after BLA photostimulation for the observed data (blue) and for control shuffled data (green). (J) Comparison of the place cell's spiking before and after the photostimulation onset for intra- and extra-field spikes. The pre/post normalised count represents decrease (positive) and increase (negative values) for the first 500- (left), 250- (middle) and 100ms (right) after the optogenetic protocol onset for the intra-field (light blue) and extra-field spikes (blue). $^{**}P < 0.01$. Error bars, mean ± s.e.m. (K) ΔCOMa for place fields located outside the ChR2 arms (extra-field) and for place cells located inside the ChR2 arms (intra-field) from ChR2 recordings (blue) and control YFP recordings (green). $^{*}P < 0.05$. Error bars, mean ± s.e.m.

Figure 7:

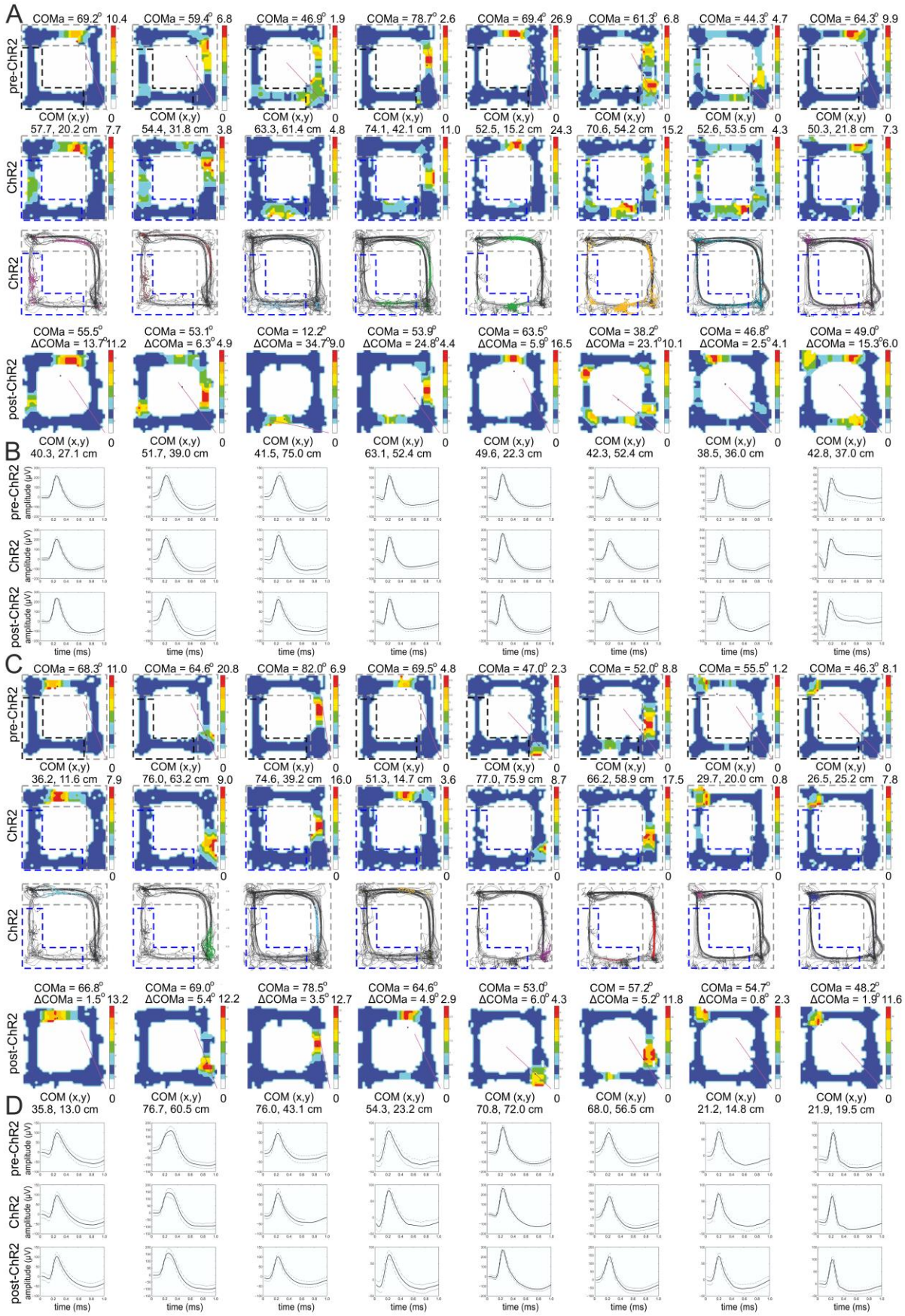
A
pre-ChR2
ChR2
ChR2
post-ChR2
B
pre-ChR2
ChR2
post-ChR2
amplitude (μV)
time (ms)
C
pre-ChR2
ChR2
ChR2
post-ChR2
D
pre-ChR2
ChR2
post-ChR2
amplitude (μV)
time (ms)

Figure 7. The degree of place field remapping depends on the extra-field spiking during BLA photostimulation. (A) Eight place cells from four rats, with fields located outside the ChR2 arms, with expressed extra-field spiking activity during the light delivery. Top panels: pre-ChR2 session, middle panels: ChR2 session, and bottom panels: post-ChR2 session. For the ChR2 session the upper panels show maps with color-coded firing rate, while the lower panels show the animal trajectory with spikes, marked with colored dots. (B) Waveforms of the place cells above, recorded from the pre-ChR2 (top row), ChR2 (middle row) and post-ChR2 session (bottom row). The solid line shows the average waveform shape; the dashed lines show the 1 SD confidence intervals. (C) Eight place cells from the same four rats, with fields located outside the ChR2 arms, with little or no extra-field spiking activity during the light delivery. (D) Waveforms of the place cells above, recorded from the pre-ChR2 (top row), ChR2 (middle row) and post-ChR2 session (bottom row). The solid line shows the average waveform shape; the dashed lines show the 1 SD confidence intervals.

Figure 8:

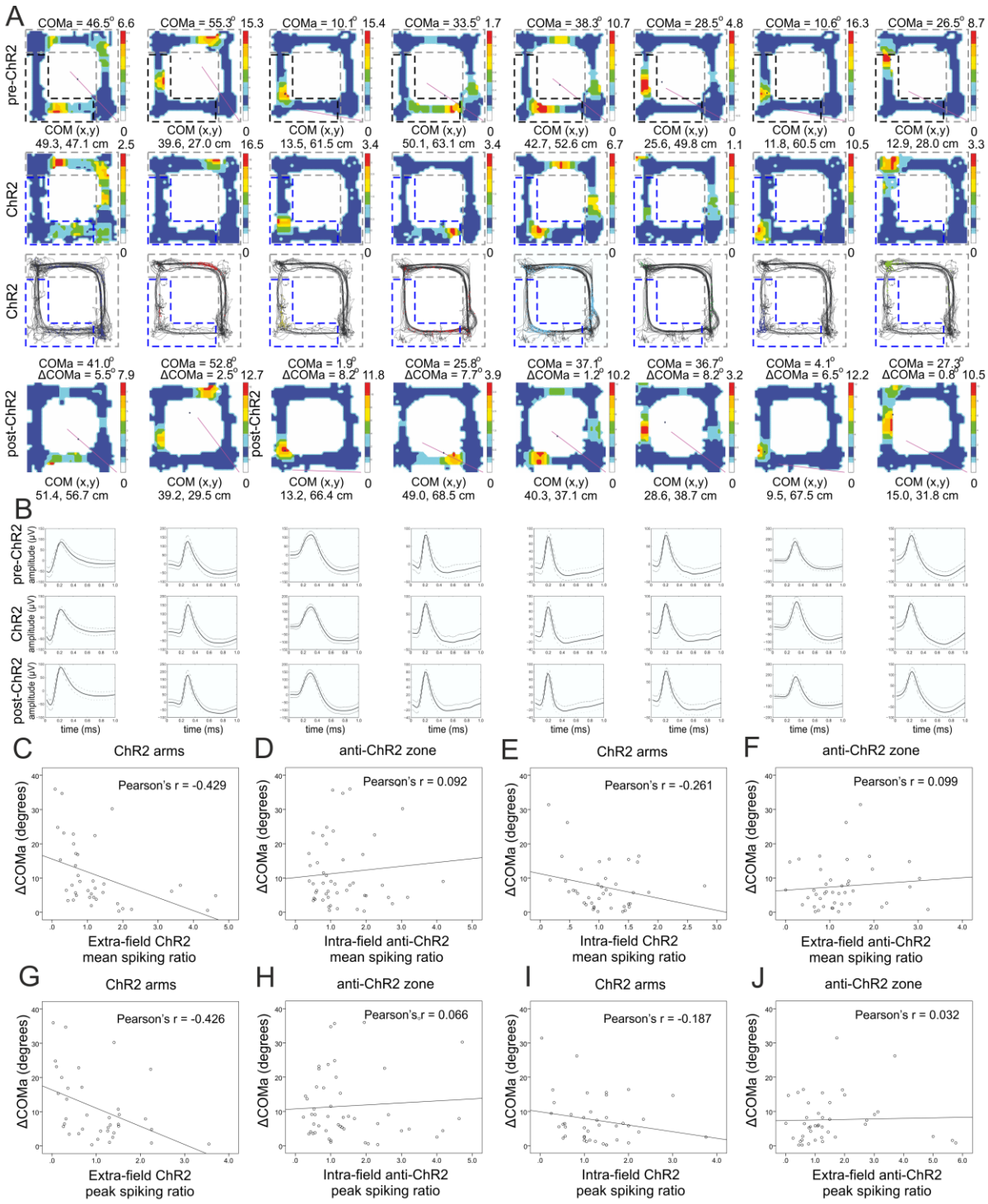
A
pre-ChR2
ChR2
ChR2
post-ChR2
B
pre-ChR2
ChR2
post-ChR2
amplitude (μV)
time (ms)
C
ChR2 arms
Pearson's r = -0.429
ΔCOMa (degrees)
Extra-field ChR2
mean spiking ratio
D
anti-ChR2 zone
Pearson's r = 0.092
Intra-field anti-ChR2
mean spiking ratio
E
ChR2 arms
Pearson's r = -0.261
Intra-field ChR2
mean spiking ratio
F
anti-ChR2 zone
Pearson's r = 0.099
Extra-field anti-ChR2
mean spiking ratio
G
ChR2 arms
Pearson's r = -0.426
Extra-field ChR2
peak spiking ratio
H
anti-ChR2 zone
Pearson's r = 0.066
Intra-field anti-ChR2
peak spiking ratio
I
ChR2 arms
Pearson's r = -0.187
Intra-field ChR2
peak spiking ratio
J
anti-ChR2 zone
Pearson's r = 0.032
Extra-field anti-ChR2
peak spiking ratio

Figure 8. BLA-triggered hippocampal spiking increase correlates to the place field center of mass shift. (A), Eight place cells from four rats, with fields located inside the ChR2 arms, with intra-field spiking during the light delivery. Top panels: pre-ChR2 session, middle panels: ChR2 session, and bottom panels: post-ChR2 session. For the ChR2 session the upper panels show maps with color-coded firing rate, while the lower panels show the animal trajectory with spikes, marked with colored dots. (B) Waveforms of the place cells above, recorded from the pre-ChR2 (top row), ChR2 (middle row) and post-ChR2 session (bottom row). The solid line shows the average waveform shape; the dashed lines show the 1 SD confidence intervals. (C) Correlation between ΔCOMa and ChR2 mean spiking ratio for the extra-field spikes of the place cells located outside the ChR2 arms. (D) Correlation between ΔCOMa and anti-ChR2 mean spiking ratio for the intra-field spikes of the place cells located inside the anti-ChR2 zone. (E) Correlation between ΔCOMa and ChR2 mean spiking ratio for the intra-field spikes of the place cells located inside the ChR2 arms. (F) Correlation between ΔCOMa and anti-ChR2 mean spiking ratio for the extra-field spikes of the place cells located outside the anti-ChR2 zone. (G) Correlation between ΔCOMa and ChR2 peak spiking ratio for the extra-field spikes of the place cells located outside the ChR2 arms. (H) Correlation between ΔCOMa and anti-ChR2 peak spiking ratio for the intra-field spikes of the place cells located inside the anti-ChR2 zone. (I) Correlation between ΔCOMa and ChR2 peak spiking ratio for the intra-field spikes of the place cells located inside the ChR2 arms. (J) Correlation between ΔCOMa and anti-ChR2 peak spiking ratio for the extra-field spikes of the place cells located outside the anti-ChR2 zone.

Figure 9:

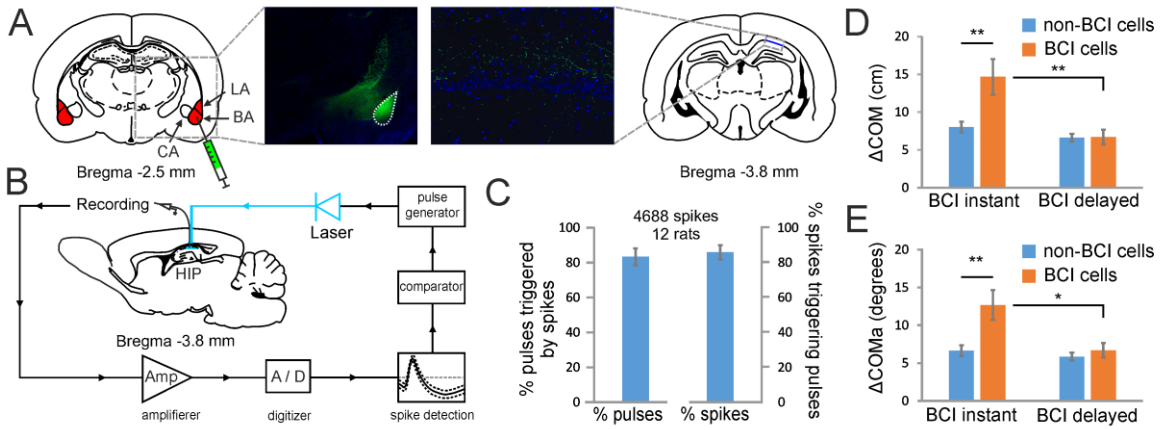

Figure 9. Closed-loop light delivery with brain-computer interface triggers spike-timed place field plasticity. (A) Left atlas schematic shows the injection site of AAV-CaMKIIα-hChR2-YFP in BLA with confocal image of BLA histology. Right atlas schematic shows the projections site in the hippocampal CA1 region with YFP-expressing fibers (green) and pyramidal cell layer in DAPI staining (blue). (B) Simplified schematics of closed-loop brain-computer interface (BCI). (C) Percent of pulses triggered by the spikes (n = 12 rats, 4688 spikes) of the selected place cells (left bar) and percent of spikes from the selected place cells that accounted for the triggered close-loop pulses (right bar). (D) Center of mass shift (ΔCOM) of non-BCI (blue) and BCI (red) place cells for instant (left) and delayed (right) close-loop photostimulation. $^{**}P < 0.01$. Error bars, mean ± s.e.m. (E) Center of mass angle shift (ΔCOMa) of non-BCI (blue) and BCI (red) place cells for instant (left) and delayed (right) close-loop photostimulation. $^{**}P < 0.01$, $^{*}P < 0.05$. Error bars, mean ± s.e.m.

Figure 10:

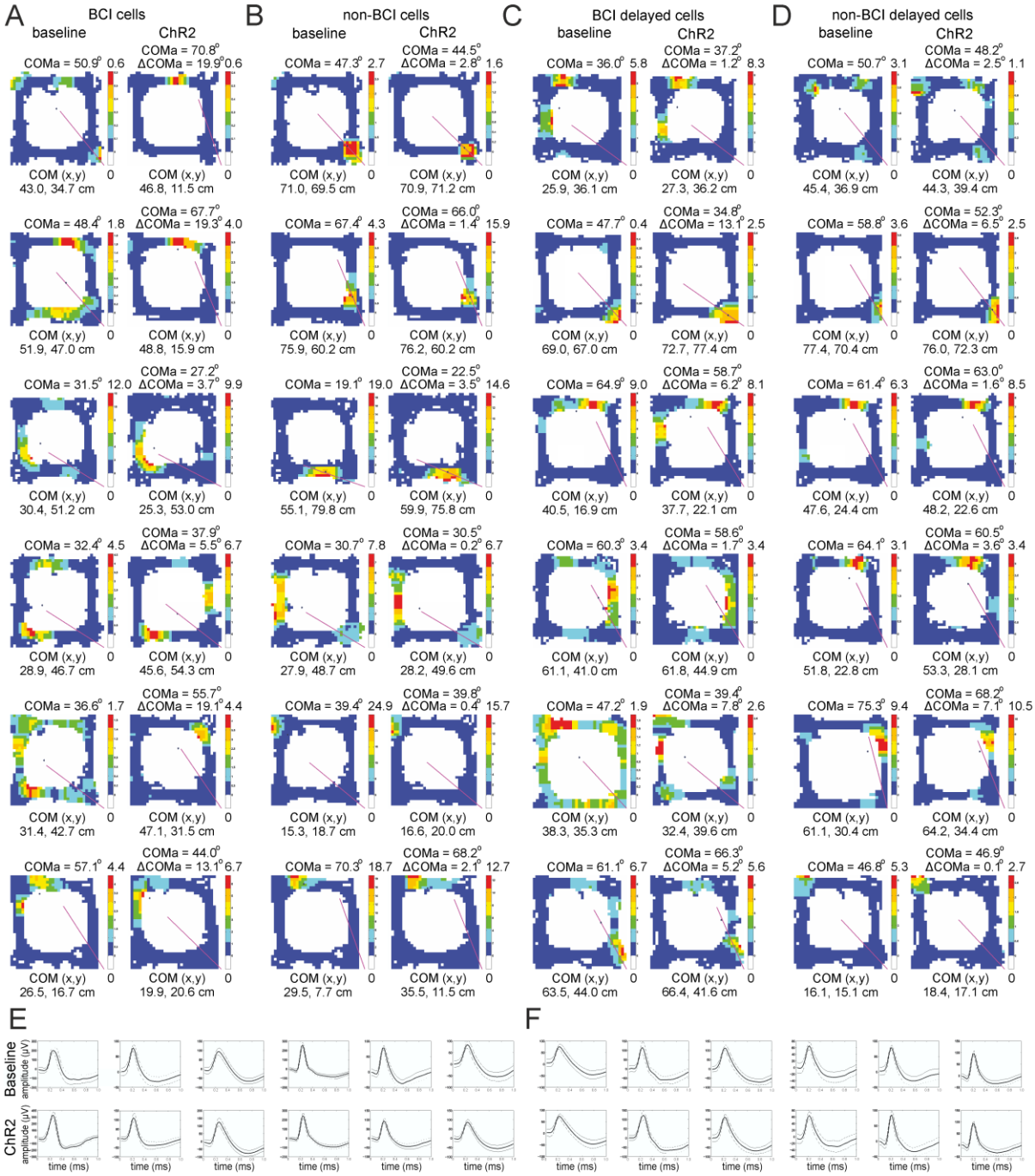

Figure 10. **Center of mass shift depends on the temporal proximity between place cell's spikes and BLA inputs activity.** (A) Field maps from the baseline (left panels) and ChR2 sessions (right panels) of BCI cells and (B) non-BCI cells from of six animals from the instant BCI group. (C) Field maps from the baseline and ChR2 sessions of BCI delayed cells and (D)

non-BCI delayed cells from of six animals from the delayed BCI group. (E) Waveforms of the BCI cells recorded from the baseline (upper row), and ChR2 session (lower row). The solid line shows the average waveform shape; the dashed lines show the 1 SD confidence intervals. (F) Waveforms of the BCI delayed cells recorded from the baseline (upper row), and ChR2 session (lower row). The solid line shows the average waveform shape; the dashed lines show the 1 SD confidence intervals.